# Integrative experimental/computational approach establishes active cellular protrusion as the primary driving force of phagocytic spreading by immune cells

Short Title: Computational analysis of immune cell spreading

Emmet A. Francis[1*], Volkmar Heinrich[1*]

[1] Department of Biomedical Engineering, University of California Davis, Davis, CA, USA

* Corresponding author

E-mail: eafrancis@ucdavis.edu (EAF), vheinrich@ucdavis.edu (VH)

# Abstract

The dynamic interplay between cell adhesion and protrusion is a critical determinant of many forms of cell motility. When modeling cell spreading on adhesive surfaces, traditional mathematical treatments often consider passive cell adhesion as the primary, if not exclusive, mechanistic driving force of this cellular motion. To better assess the contribution of active cytoskeletal protrusion to immune-cell spreading during phagocytosis, we here develop a computational framework that allows us to optionally investigate both purely adhesive spreading ("Brownian zipper hypothesis") as well as protrusion-dominated spreading ("protrusive zipper hypothesis"). We model the cell as an axisymmetric body of highly viscous fluid surrounded by a cortex with uniform surface tension and incorporate as potential driving forces of cell spreading an attractive stress due to receptor-ligand binding and an outward normal stress representing cytoskeletal protrusion, both acting on the cell boundary. We leverage various model predictions against the results of a directly related experimental companion study of human neutrophil phagocytic spreading on substrates coated with different densities of antibodies. We find that the concept of adhesion-driven spreading is incompatible with experimental results such as the independence of the cell-spreading speed on the density of immobilized antibodies. In contrast, the protrusive zipper model agrees well with experimental findings and, when adapted to simulate cell spreading on discrete adhesion sites, it also reproduces the observed positive correlation between antibody density and maximum cell-substrate contact area. Together, our integrative experimental/computational approach shows that phagocytic spreading is driven by cellular protrusion, and that the extent of spreading is limited by the density of adhesion sites.

# Author Summary

To accomplish many routine biological tasks, cells must rapidly spread over different types of surfaces. Here, we examine the biophysical underpinnings of immune cell spreading during phagocytosis, the process by which white blood cells such as neutrophils engulf pathogens or other foreign objects. Our computational framework models the case in which a human neutrophil spreads over a flat surface coated with antibodies, which we also test experimentally in a companion paper. Our primary purpose is to assess whether phagocytic spreading is actively driven by protrusive forces exerted by the cell, or passively by adhesive forces acting between receptors in the cell membrane and antibodies on the surface. By directly comparing our model predictions to experimental results, we demonstrate that phagocytic spreading is primarily driven by protrusion, but the extent of spreading is still limited by the availability of binding sites. Our findings improve the fundamental understanding of phagocytosis and may also pave the way for future investigations of the balance between adhesion and protrusion in other forms of cell spreading, such as wound healing or cancer cell migration.

# Introduction

The ability of cells to spread on surfaces is critical to many biological processes, including cell migration, wound healing, and tissue formation. Immune cells are especially adept at rapid spreading; for instance, neutrophils commonly travel up to an order of magnitude faster in motility assays than fibroblasts or endothelial cells [1-5]. Vital immune cell functions, such as firm arrest at the endothelium and phagocytosis of pathogens, rely on this ability. A deeper understanding of the physical mechanisms driving cell spreading is essential for informed pharmaceutical strategies and new therapies targeting immune cells, such as current efforts to enhance phagocytosis for more effective clearance of cancer cells [6, 7].

Many experimental and theoretical studies have sought to unravel the physical principles of cell spreading by analyzing the initial growth of cell contact regions on a flat, adhesive substrate [8-11]. However, it often remains unclear whether any given type of cell spreading is primarily driven by passive forces due to adhesion or by active protrusive and/or contractile forces generated by the cell. In the simplest model, cell spreading is treated as a purely passive process, similar to a viscous droplet spreading on an adhesive substrate [8, 12, 13]. Alternative models assume that cytoskeleton-driven protrusion determines the rate of cell spreading, neglecting the effective attractive force due to ligand-receptor binding [10, 14, 15].

Here, we aim to illuminate fundamental cell-spreading mechanisms by focusing on phagocytic spreading. In conventional phagocytosis, an immune cell first adheres to the surface of a target particle such as a bacterium, often by binding to opsonic ligands such as immunoglobulin G (IgG) antibodies. The cell then spreads over the target surface until its membrane closes around the particle. On the other hand, when presented with an excessively

83 large target, the cell is unable to fully engulf the particle and continues to spread until its target-
84 contact area reaches a maximum [16, 17]. Such cases, including phagocytic spreading on flat
85 substrates, are termed frustrated phagocytosis. The relatively simple geometry of a cell
86 undergoing frustrated phagocytic spreading on a flat surface is particularly amenable to
87 theoretical analysis, especially when the cell spreads in an axisymmetric manner.

88 Reflecting the above-mentioned contrasting mechanistic notions about generic cell
89 spreading, two hypotheses have been put forward to explain phagocytic spreading, i.e., the
90 "Brownian zipper" and "protrusive zipper" models [18]. Both models concur that fresh contact
91 between the cell membrane and target surface results in a zipper-like adhesive attachment that is
92 essentially irreversible. However, regarding the driving force of cellular advancement, the
93 Brownian zipper model postulates that strong adhesion alone is responsible for pulling the cell
94 membrane onto the target surface. In contrast, the protrusive zipper model assumes that the
95 cytoskeleton actively generates protrusive force to push the front of the cell outwards.

96 We seek to establish which of these hypotheses is more realistic by developing
97 mathematical models of the mechanics of isotropic cell spreading and comparing our theoretical
98 predictions with experimental observations of human neutrophils spreading on flat, IgG-coated
99 surfaces. As reported in detail in a companion paper, our experimental design allowed us to
100 examine the spreading behavior of neutrophils on surfaces coated with different densities of IgG
101 [19]. Because higher IgG densities correspond to stronger adhesive forces, we reasoned that the
102 Brownian zipper model should predict a much stronger correlation between IgG density and rate
103 of contact-area growth ("spreading speed") than the protrusive zipper model. Here, we use
104 computer simulations of phagocytic spreading to verify this common-sense expectation and
105 further investigate mechanisms governing immune-cell spreading. Together, our integrative

experimental/theoretical approach establishes that the Brownian zipper model is inconsistent with experimental results, whereas the spreading dynamics predicted by the protrusive zipper model agree well with our experiments.

# Results

## Model implementation of key biophysical mechanisms of cell spreading

We consider a simple model cell that captures the basic geometrical and mechanical properties of human neutrophils, the most abundant type of white blood cell and one of the prototypes of professional phagocytes. This model cell consists of an axisymmetric, highly viscous fluid body of constant volume that is surrounded by an elastic cortex with uniform tension (Fig 1). Termed the "cortical shell, liquid core model", this theoretical concept has successfully reproduced the passive response of human neutrophils to imposed deformations [20-22]. In the undeformed reference state, the persistent tension of the cortex maintains a spherical cell shape with a typical diameter of 8.5 μm. The nucleus of neutrophils is segmented into three to five lobes and appears to play only a minor role during deformations, lending support to the approximation of the cell interior as a homogeneous fluid. The effective viscosity ($\mu$) of the cytoplasm has been found to be about 200,000 times the viscosity of water at room temperature in passive neutrophils [20, 21], and another ~3-times higher in active neutrophils [23]. It is well known to increase during phagocytosis [24-26]. We use a viscosity value of $\mu$ = 200 Pa-s in our passive Brownian zipper model and a value of $\mu$ = 1660 Pa-s in our active protrusive zipper model. The original

assumption of a constant cortical tension [20, 22] was later found to be approximately true only for small deformations. The revised relationship between tension ($\tau$) and cell surface area ($A_{cell}$) was shown to be roughly biphasic [27]. Assuming an isotropic and uniform tension, and in overall agreement with a number of quantitative experimental studies [24, 27, 28], our simulations incorporate a smoothed version of the following biphasic constitutive relationship:

$$\tau(A_{cell}) = \begin{cases} 0.01 + 0.16\left(\dfrac{A_{cell}}{A_{cell,0}} - 1\right)\dfrac{\mathrm{mN}}{\mathrm{m}} & \text{if} \quad \dfrac{A_{cell}}{A_{cell,0}} \le 1.26 \\ 0.0516 + 0.545\left(\dfrac{A_{cell}}{A_{cell,0}} - 1.26\right)\dfrac{\mathrm{mN}}{\mathrm{m}} & \text{if} \quad \dfrac{A_{cell}}{A_{cell,0}} > 1.26 \end{cases} \tag{1}$$

Where $A_{cell,0}$ is the surface area of the resting neutrophil before spreading.

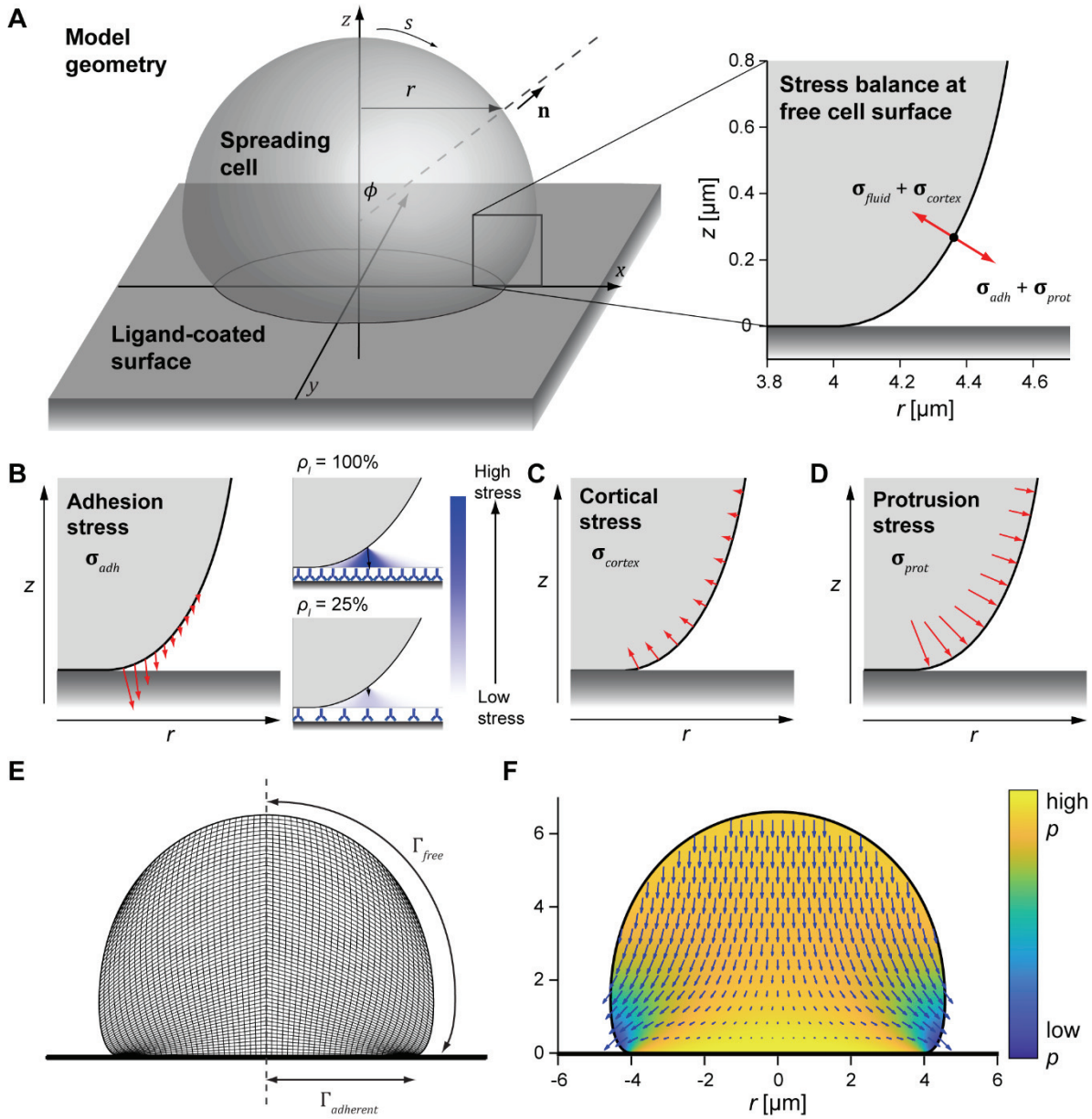


**Fig 1. Illustration of our computational model of isotropic cell spreading.**

(A) 3D rendering shows the geometry and defines coordinates for an axisymmetric spreading cell on a flat surface. The enlarged inset (right) illustrates the stress balance at the free cell boundary. (B) Adhesion stress effectively pulls the membrane onto the flat surface. The enlarged insets conceptually depict how the adhesion stress is computed for different ligand densities $\rho_l$. (C) Cortical tension and membrane curvature give rise to an effective inward normal stress. (D)

141 The protrusion stress acts normal to the cell membrane and is concentrated at the region of the
142 membrane closest to the substrate. (E) The cross-sectional snapshot of a simulation illustrates the
143 mesh composed of quadrilateral elements used in the calculations, with tighter element packing
144 closer to the flat surface. The computational domain only includes half of this mesh due to axial
145 symmetry. Boundary regions are labeled $\Gamma$, and the vertical dashed line is the symmetry axis ($r$
146 = 0) (F) This snapshot of a simulation illustrates the fluid velocity (vector field) and relative
147 pressure (heat map) computed for a given cell shape with known boundary stresses.

148

149 Movements of the viscous cytoplasm generally do not exceed velocities of 1 μm/s during
150 phagocytic cell spreading and are characterized by low Reynolds numbers. Such movements are
151 well described by the Stokes equations for creeping flow:

152 $$\mu \nabla^2 \mathbf{v} = \nabla p \tag{2}$$

153 along with the continuity equation for incompressible fluids:

154 $$\nabla \cdot \mathbf{v} = 0 \tag{3}$$

155 Here, $\mathbf{v}$ denotes the fluid velocity vector, and $p$ is fluid pressure. Together, these equations
156 govern the flow behavior of our model cell.

157 Interactions between the cell surface and the substrate can facilitate cell spreading
158 directly via adhesion, and indirectly through receptor-induced signaling that leads to protrusion.
159 Including the respective stresses, the moving boundary condition governing the free (i.e.,
160 nonadherent) part of the cell surface ($\Gamma_{free}$) balances up to four types of stress vectors: fluid stress
161 ($\boldsymbol{\sigma}_{fluid}$), adhesion stress ($\boldsymbol{\sigma}_{adh}$), protrusion stress ($\boldsymbol{\sigma}_{fluid}$), and cortical stress ($\boldsymbol{\sigma}_{cortex}$) (Fig 1A):

162 $$\boldsymbol{\sigma}_{fluid} + \boldsymbol{\sigma}_{adh} + \boldsymbol{\sigma}_{cortex} + \boldsymbol{\sigma}_{prot} = \mathbf{0} \quad \text{on } \Gamma_{free} \tag{4}$$

The fluid stress vector $\boldsymbol{\sigma}_{fluid}$ encompasses the pressure difference across the cell surface as well as the stress exerted on the surface by the moving cytoplasm. It is determined by the constitutive relation for a Newtonian fluid:

$$\boldsymbol{\sigma}_{fluid} = \boldsymbol{\sigma}_{fluid,out} - \boldsymbol{\sigma}_{fluid,in} = (p - p_{out})\mathbf{n} - \mu\left(\nabla\mathbf{v} + (\nabla\mathbf{v})^T\right)\cdot\mathbf{n} \tag{5}$$

where $\mathbf{n}$ is the unit surface normal, and the dot in the last term on the right-hand side denotes the inner product between a tensor and a vector. The extracellular medium has a much lower viscosity than the intracellular fluid; therefore, Eq (5) neglects the medium's viscous contribution and only accounts for its hydrostatic pressure denoted $p_{out}$.

Our implementation of the adhesion stress is based on the assumption that adhesion can effectively be represented by a short-range attractive potential between the cell surface and the ligand-coated substrate. We compute the effective adhesion stress at a given point on the cell surface by summing over all pairwise interactions with substrate molecules that lie outside the cell-substrate contact region at the time (Fig 1B). For a continuum of ligand molecules, the resulting expression takes the form (derived in S6 Appendices)

$$\boldsymbol{\sigma}_{adh} = \sigma_o \rho_l \iint_{\text{substrate}} \mathbf{f}_{unit}\left[\left(\frac{D_0}{D}\right)^7 - \left(\frac{D_0}{D}\right)^4\right] dA \tag{6}$$

where $\rho_l$ is the ligand surface density and $\sigma_0$ is a scaling factor representing the strength of interaction per unit area of the cell surface. The unit vector $\mathbf{f}_{unit}$ specifies the direction of a given interaction, $D$ denotes the distance between the interacting points, and $D_0$ is a constant setting the overall range of the adhesion potential (set to 50 nm in our simulations).

The origin of the cortical stress is the cortical tension, which resists expansion of the cell surface area and acts along the curved surface of the cell (Fig 1D). The resulting stress acts

184 normal to the surface and is given by the product of the tension $\tau$ and the mean curvature of the

185 cell surface, as dictated by Laplace's law:

186 $$\boldsymbol{\sigma}_{cortex} = -\tau\left(\frac{\partial\phi}{\partial s} + \frac{\sin\phi}{r}\right)\mathbf{n} \tag{7}$$

187 Here, the term in parentheses is the mean curvature of the axisymmetric cell surface expressed in

188 the coordinates defined in Fig 1A.

189 The protrusion stress comprises outward forces exerted on the cell surface by the actively

190 remodeling cytoskeleton. Purposeful reorganization of intracellular structures requires tight

191 coordination by biochemical signaling cues, which in turn are induced by receptor-ligand

192 binding. Rather than attempting to implement these highly complex mechano-chemical

193 mechanisms, we capture their localized character in a semiempirical manner. Our model

194 postulates that the protrusive stress is greatest at the perimeter of the cell-substrate contact region

195 and decays as a function of the distance from this leading edge measured along the arc length ($s$,

196 Fig 1A) of the contour of the unbound cell surface. We assume that this stress acts normal to the

197 cell boundary, and that its decay along the free cell surface is exponential (Fig 1C):

198 $$\boldsymbol{\sigma}_{prot} = \sigma_{prot} e^{-\frac{s_{contact} - s}{s_0}} \mathbf{n} \tag{8}$$

199 In this equation, $s_{contact}$ is the arc length value at which the cell-surface contour makes contact

200 with the substrate, and $s_0$ is the characteristic length that sets the spatial range of the protrusion

201 stress.

202 Bearing in mind that cytoskeletal remodeling also is responsible for the behavior of the

203 cortical tension, and that the tension varies during cell spreading (Eq (1)), it is reasonable to

204 assume that the overall strength of the protrusion stress ($\sigma_{prot}$) varies in a similar fashion. In

205 addition to the spatial distribution of the cortical stress governed by Eq (8), we therefore also
206 postulate a deformation-dependent strength of the protrusive stress. Our choice of this
207 dependence, and its motivation, will be explained in a later section.

208 Finally, for the part of the cell surface that is in contact with the substrate, we enforce a
209 simple no-slip boundary condition, requiring that

210 $$\mathbf{v} = \mathbf{0} \quad \text{on } \Gamma_{adherent} \tag{9}$$

211 Each simulation begins with a model cell that rests on the surface and has formed a very
212 small initial contact footprint (area < 0.1 $\mu m^2$). The shape of the upper, free part of the cell at this
213 time is a spherical cap. We determine the fluid velocities and pressure distribution at each time
214 step by solving a perturbed form of the Stokes equations using the finite element method (FEM;
215 Fig 1E,F) as described previously [29]. We then use the computed velocities to evolve the cell
216 shape over a small time step. Details of our model implementation and solution method are given
217 in Methods and S6 Appendices.

218 This generic modeling framework of cell spreading can easily be adopted to represent
219 different mechanistic notions by adjusting the relative contributions of the adhesion and
220 protrusion stresses. Disregarding the protrusion stress altogether results in a mathematical
221 representation of the Brownian zipper model described in the Introduction. On the other hand,
222 the protrusive zipper model generally includes both the protrusion stress as well as the adhesion
223 stress. A purely protrusion-driven mode of spreading also can be tested by setting the adhesion
224 stress to zero, although one needs to bear in mind that irreversible adhesion still maintains the
225 cell-substrate contact region in this case. In all model versions, the adhesion stress can be varied
226 over several orders of magnitude to predict how the spreading behavior depends on the density
227 of ligand displayed on the substrate.

228

229 # Quantitative experimental results for the validation of model
230 versions

231 The computational framework presented in the previous section can be adopted to
232 simulate interactions by various cell types with targets of different axisymmetric geometries. Our
233 present focus on human neutrophils spreading on flat substrates is motivated by a wealth of
234 experimental results obtained for this particular scenario and presented in a companion paper
235 [19]. In brief, we exposed cells to glass coverslips coated with IgG antibodies at densities ($\rho_{IgG}$)
236 spanning ~3 orders of magnitude. The analysis of these highly controlled experiments included
237 measurements of the cell-substrate contact area of spreading cells over time (Fig 2). Regardless
238 of IgG density, we found that the area-versus-time curves typically were sigmoidal in shape (Fig
239 2B,C). Defining a cell's "spreading speed" as the fastest rate of contact-area growth (i.e., the
240 slope of a sigmoidal fit to the area-versus-time curve at the inflection point), we found that all
241 spreading cells increased their substrate-contact area at speeds of around 3 $\mu m^2/s$ irrespective of
242 the density of deposited IgG (Fig. 2D). The measured values of the maximum contact area of
243 spreading cells, on the other hand, exhibited a moderate but significant increase at higher IgG
244 densities (Fig 2E). These experimental results provide useful quantitative benchmarks for
245 comparison with computer simulations and will be used in the following sections to evaluate the
246 validity of different mechanistic notions about cell spreading.

247

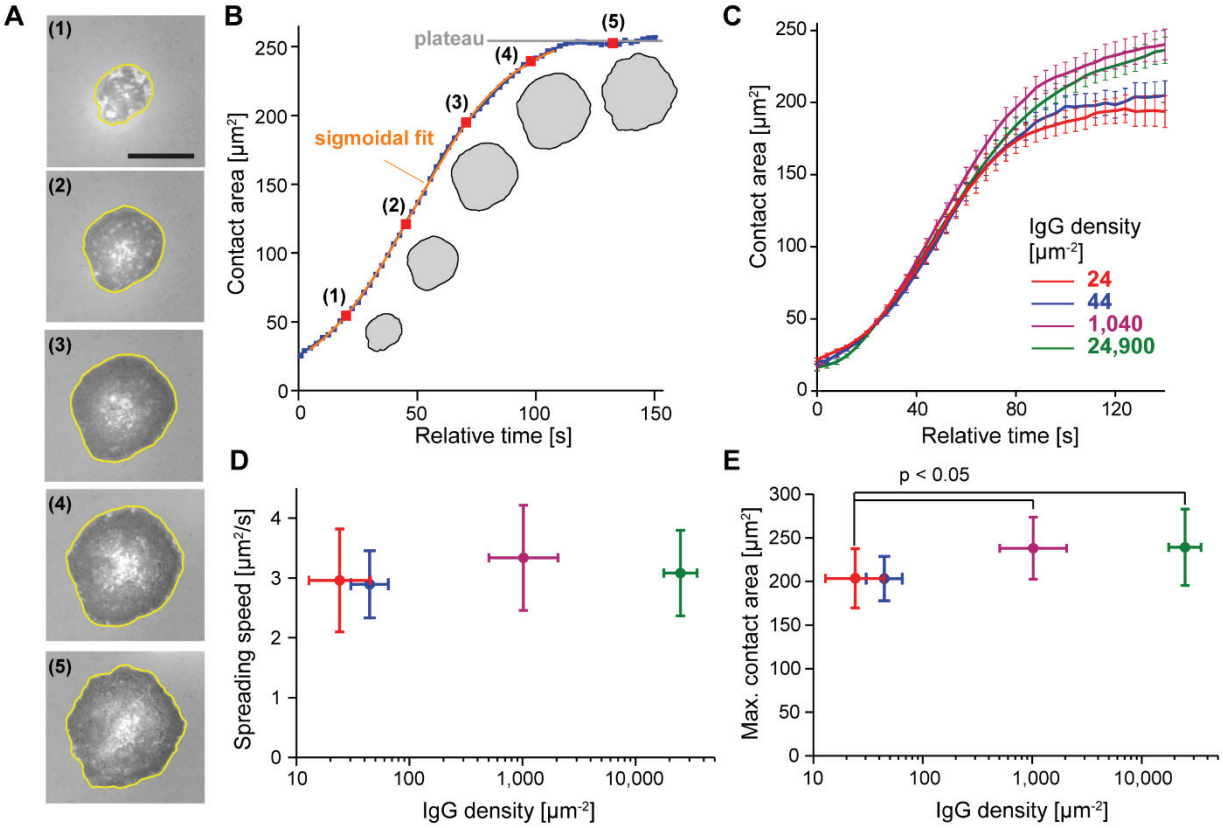


248 **Fig 2. Summary of experimental results.**

249 (A) The contact region of a spreading neutrophil was imaged using reflection interference
250 contrast microscopy (RICM). Contact regions in this example are traced in yellow. The scale bar
251 in the first image denotes 10 μm. (B) Contact area is plotted as a function of time for the
252 spreading cell shown in (A). The spreading speed is defined as the maximum slope extracted
253 from a sigmoidal fit, and the maximum contact area is given by averaging the contact area at the
254 plateau. (C) Mean contact area is computed at discrete time values for aligned curves of cells
255 spreading on different densities of IgG. Mean quantified IgG densities are reported in the figure
256 legend as IgG molecules per $\mu m^2$. Error bars represent standard error of the mean. (D) Average
257 spreading speed was quantified for the different IgG densities. There is no significant difference
258 between mean slope values. (E) Maximum contact area increases slightly as a function of IgG
259 density. Statistically significant differences in maximum contact area values were verified using

260 ANOVA followed by a Tukey post hoc test. Error bars in both (D) and (E) indicate standard
261 deviation. The IgG density was quantified for each condition as described in [19].

262

263 An additional measure of interest can be inferred from the actual surface densities of IgG
264 used in the experiments. The most densely coated coverslips presented about 25,000 IgG
265 molecules per $\mu m^2$ and induced ~85% of deposited cells to spread. Remarkably, even at a low
266 IgG surface density of ~44 molecules per $\mu m^2$, about 30% of the deposited cells still spread in an
267 IgG-dependent manner. Assuming that all IgG molecules in the cell-substrate contact region
268 have formed bonds with the cell's Fcγ receptors, and using an average equilibrium constant of
269 $10^{-6}$ M for these receptor-ligand bonds [30], conservative (upper-limit) estimates of the adhesion
270 energy density of cell-substrate interactions on substrates coated with the high and low numbers
271 of IgG yield 1,500 $\mu J/m^2$ and 2.6 $\mu J/m^2$, respectively.

272

## 273 Purely adhesion-driven spreading: predictions by the Brownian 274 zipper model

275 We first tested the simplest version of our framework, the Brownian zipper model, by
276 simulating purely adhesion-driven spreading in the absence of any protrusion stress (Fig 3, S1
277 Movie). In this scenario, the model cell is passive and is pulled onto the substrate by short-range
278 attraction. This case is conceptually equivalent to a viscous droplet spreading on an adhesive
279 substrate.

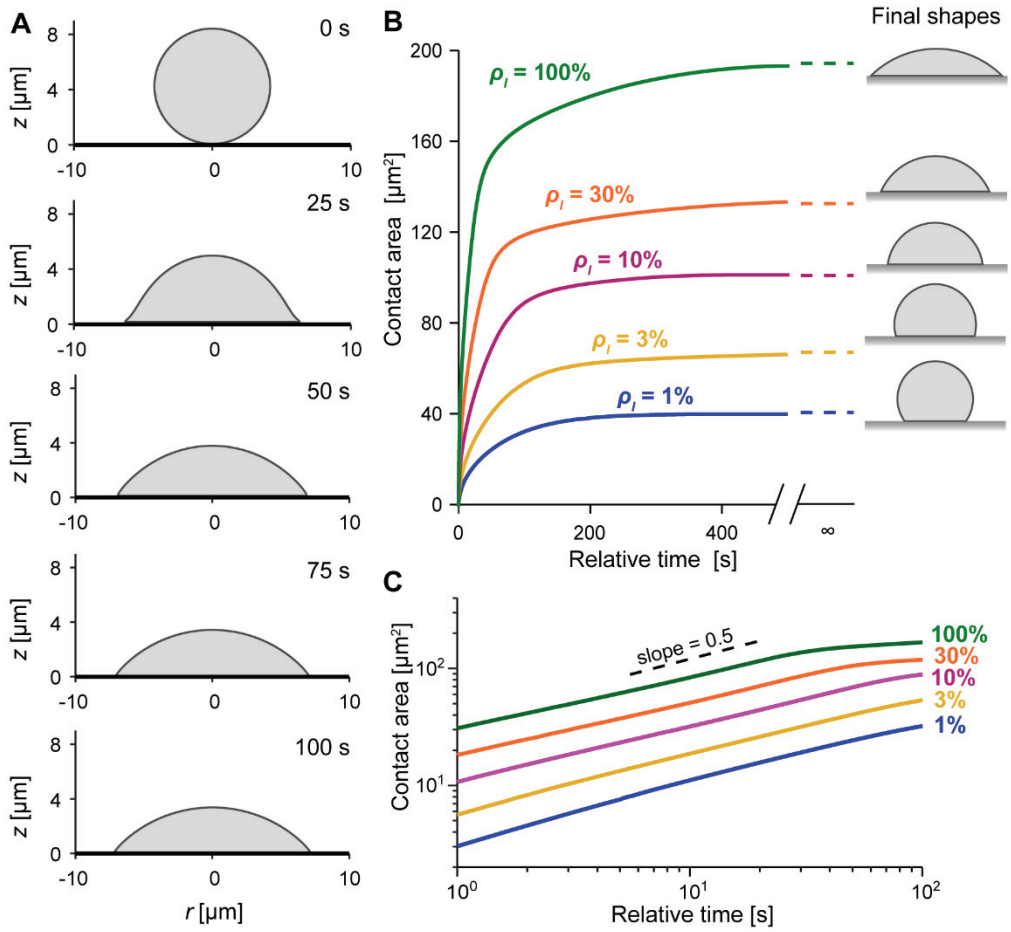


**Fig 3. Predictions of the Brownian zipper model.**

(A) A model cell spreading on the highest tested ligand density (100%) quickly approaches a spherical cap morphology. Time stamps are included for each snapshot. (B) Curves of contact area vs. time show that the spreading rate decreases monotonically. The contact area ultimately approaches steady-state values predicted by the Young-Dupre equation (dashed lines). Predicted equilibrium shapes are included on the right. (C) Log-log plot of contact area vs. time is nearly linear over the initial spreading phase. The slope of this line corresponds to the exponent of a power law describing contact area growth as a function of time. The dashed line shows a slope of 0.5 for reference.

290

291 Varying the ligand density $\rho_l$ over two orders of magnitude, we found that the model
292 cells generally spread fastest immediately after first contacting the substrate. Afterwards, the
293 growth rate of the cell-substrate contact area decreased monotonically until the contact area
294 reached a steady-state plateau marking equilibrium (Fig 3B). As expected, the equilibrium
295 shapes were spherical caps. Log-log plots of the contact-area-versus-time predictions during the
296 initial, fast spreading phase were approximately linear, with slopes close to 0.5 (Fig 3C). Hence,
297 the contact-area growth initially obeys a power law, in agreement with various laws proposed to
298 describe droplet wetting dynamics [31] or passive cell spreading [8, 13]. In fact, the exponent of
299 0.5 is an excellent match to results of a previous study that modeled cells as highly viscous
300 droplets [13]. In S6 Appendices, Appendix B, we show how this exponent naturally arises during
301 early spreading of a passive model cell driven by adhesion stresses concentrated at the contact
302 perimeter.

303 Although the predictions of the Brownian zipper model agree well with the typical
304 theoretical behavior expected for this kind of passive model cell, they clearly differ from the
305 results of our phagocytic spreading experiments (Fig 2) in several important ways. First, the
306 simulated contact-area-versus-time curves lack the characteristic sigmoidal shapes observed in
307 experiments. Second, the predicted spreading curves exhibit a very strong dependence on the
308 density of encountered ligands, in stark contrast to the observed spreading behavior. This
309 dependence is evident in both the predicted spreading speeds, which increase dramatically with
310 ligand density, as well as the predicted maximum contact areas, which increase several-fold as a
311 function of the tested adhesive strengths.

312 Finally, the equilibrium shapes obtained for the adhesion energy densities used in the
313 simulations are inconsistent with the cell deformations observed on the experimentally tested
314 IgG densities. At equilibrium, the adhesion energy density ($\gamma$) of the Brownian zipper model cell
315 is related to the cortical tension $\tau$ and the contact angle $\theta_c$ via the Young-Dupre equation (Fig
316 4):

317 $$\gamma = \tau(1 - \cos\theta_c) \quad (10)$$

318 For a given value of the maximum cell-substrate contact area $A_c$, the equilibrium shape of the
319 model cell—a spherical cap—is uniquely defined by $A_c$ and the known, constant cell volume.
320 Thus, basic geometry allows us to calculate the contact angle $\theta_c$ as well as the total cell surface
321 area $A_{cell}$. Inserting the value of the latter into Eq (1) provides the cortical tension at equilibrium,
322 which then can be used in Eq (10) to obtain the adhesion energy density as a function of $A_c$ (Fig
323 4). As expected, the relationship between maximum contact area and adhesion strength predicted
324 by our numerical simulations agrees well with the Young-Dupre equation (Fig 3B, Fig S2 in S6
325 Appendices). The quantitative comparison of this theoretical prediction to actual adhesion energy
326 densities—estimated from the densities of deposited IgG molecules as explained earlier—
327 exposes entirely different behaviors between the model and experiments, however (Fig 4).
328 Especially in experiments performed at lower IgG densities, the conservatively estimated
329 adhesion energy densities were much lower than what would be required to form the measured
330 maximum contact areas solely by adhesion. In summary, the results of this section rule out
331 adhesion as the primary driving force of frustrated phagocytic spreading.

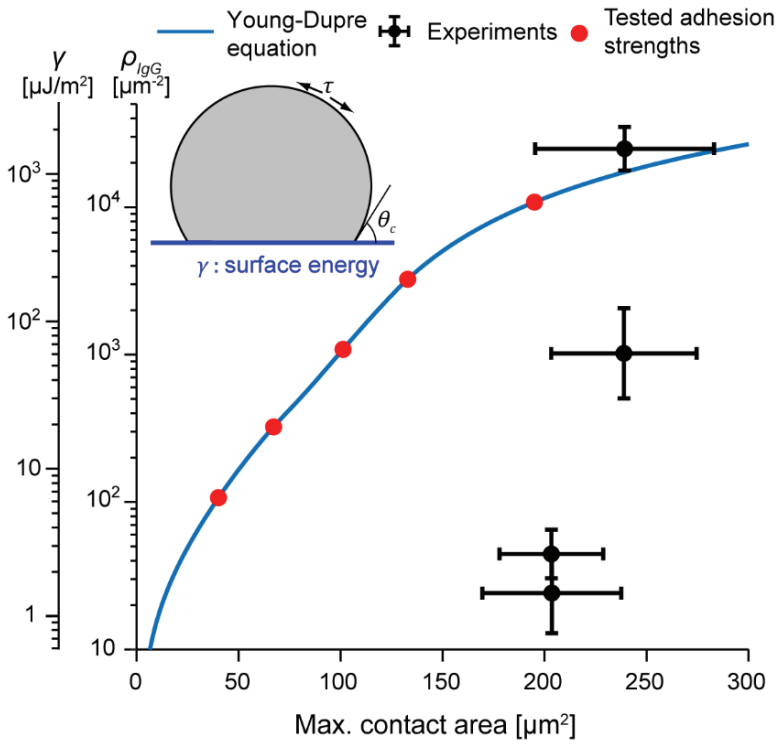


**Fig 4. Relationship between ligand density and maximum contact area, as predicted by the Young-Dupre equation.**

The adhesion energy $\gamma$, and therefore the ligand density $\rho_{IgG}$, can be expressed as a function of the contact area of the final spherical cap formed by a viscous droplet. The tested adhesion strengths are marked as red dots. Actual experimental values are shown for comparison. Error bars indicate standard deviation.

# Protrusion-dominated spreading: predictions of the protrusive zipper model

The protrusive zipper model incorporates the protrusion stress into the basic framework considered in the previous section, enabling us to account for active force generation by the

model cell. Our semiempirical implementation is motivated by biological plausibility, and by the goal to reproduce experimental observations with a minimum set of rules for the spatial distribution (Eq (8)) and the deformation-dependent evolution of the protrusion stress during cell spreading. To capture the presumed correlation between receptor-induced signaling and protrusive force generation by the cytoskeleton, we express the strength of the protrusion stress as a function of the cell-substrate contact area $A_c$. We assume that in the initial low-tension regime, the protrusion stress grows linearly with $A_c$. Once the cortical tension increases more steeply, the protrusion stress is assumed to grow faster as well. Ultimately, the strength of the protrusion stress levels out at a maximum value of $\sigma_{prot,max} = 3.5$ kPa, within the range of experimentally measured stresses exerted by parallel actin filaments [32, 33]. This behavior is implemented in our model through a smoothed version of the following rule:

$$\sigma_{prot} = \sigma_{prot,max} \times \begin{cases} \left[0.05 + 0.3\left(\dfrac{A_c}{A_{c,trans}}\right)\right] & \text{if} \quad \dfrac{A_{cell}}{A_{cell,0}} \le 1.26 \\ \left[0.35 + 0.65\left(\dfrac{A_c - A_{c,trans}}{120\ \mu\text{m}^2}\right)^{1/2}\right] & \text{if} \quad \dfrac{A_{cell}}{A_{cell,0}} > 1.26 \text{ and } A_c \le A_{c,trans} + 120\,\mu\text{m}^2 \\ 1 & \text{if} \quad A_c > A_{c,trans} + 120\,\mu\text{m}^2 \end{cases} \quad (11)$$

where $A_{c,trans}$ is the contact area when the total cell surface area $A_{cell}$ is equal to $1.26A_{cell,0}$, the transitional moment when the cortical tension starts rising more rapidly (Eq (1)).

We started examining the behavior of this model by first disregarding the adhesion stress altogether. In this scenario, cell spreading is driven solely by protrusion, and the only role of adhesion is to render cell-substrate contacts irreversible. We found that in this case, the model cell begins spreading slowly while a distinctive leading edge gradually develops (Fig 5A, S2 Movie), resulting in a morphology that clearly differs from the spherical caps predicted by the

363 Brownian zipper model (Fig 3). Spreading slows noticeably at about 90 s, around the time the
364 protrusion stress reaches its maximum value. The resulting contact-area-versus-time curve has a
365 sigmoidal shape (Figure 5B,C). Plots of the protrusion stress and the cortical tension as a
366 function of time illustrate the qualitatively similar evolution of these two quantities, with the rise
367 of the tension lagging due to the initial "slack" of the cell surface in the low-tension regime (Eq
368 (1)).

369

370

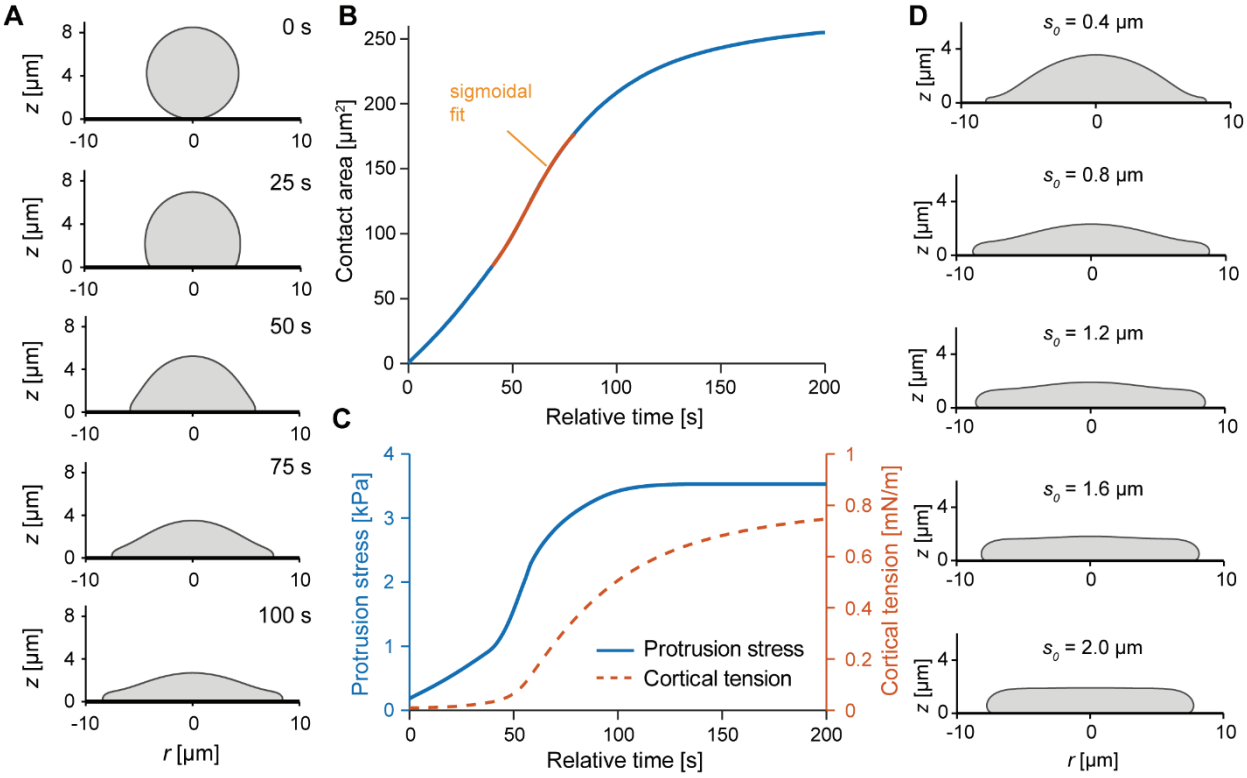


371 **Fig 5. Predictions of the protrusive zipper model.**

372 (A) For purely protrusion-driven spreading, lamellar pseudopods form as the protrusion stress
373 increases over time. Time stamps are shown for the sample images. (B) Contact area increases
374 sigmoidally over time for the protrusive zipper model. The slope of the sigmoidal fit here is 3.0
375 $\mu m^2/s$ at the inflection point, which matches the average spreading speed observed

experimentally. (C) Protrusion stress (governed by Eq (11)) and cortical tension (governed by Eq (1)) increase during cell spreading. (D) Varying the parameter $s_0$ determines the thickness of the pseudopods, with skinny protrusions for $s_0$ = 0.4 μm (top) and coordinated global cell deformation at $s_0$ = 2.0 μm (bottom); all sample profiles are shown at t = 120 s. For the protrusive zipper simulations shown in all other cases, we used $s_0$ = 0.8 μm.

We chose the value $s_0$ = 0.8 μm for the characteristic length that defines the spatial range of the protrusion stress (Eq (8)) in the simulations shown in Fig 5A-C. Because $s_0$ does not appear to be a directly measurable quantity, it is instructive to inspect how its value affects the spreading model cell. Snapshots from simulations using different values of $s_0$ demonstrate how the cell morphology (here: at 120 s) depends on the spatial range over which the protrusion stress acts (Fig 5D, S3 Movie). Unsurprisingly, the leading edge of the cell assumes the shape of a thin lamella for small values of $s_0$ and becomes increasingly thicker at larger $s_0$-values. We note though that aside from this varying thickness of cellular protrusions, the overall spreading behavior is similar across different values of $s_0$.

We next repeated the simulation with the same settings as used for Fig 5 but now also included the adhesion stress. We again examined the same set of adhesion strengths as used in our tests of the Brownian zipper model (Fig 3). The simulations expose how, in this scenario, cell-substrate adhesion promotes spreading, affecting the overall spreading behavior in a quantitative manner but without altering it qualitatively. The model cells spread somewhat faster and farther on substrates coated with higher ligand densities (Fig 6A), with slightly larger contact angles between their leading edge and the substrate (Fig 6B, S4 Movie). However, the sigmoidal character of the contact-area-versus-time curves is conserved through most of the tested adhesion

strengths, and both the spreading speeds as well as the maximum contact areas vary much less than in the predictions of the Brownian zipper model (Fig 3).

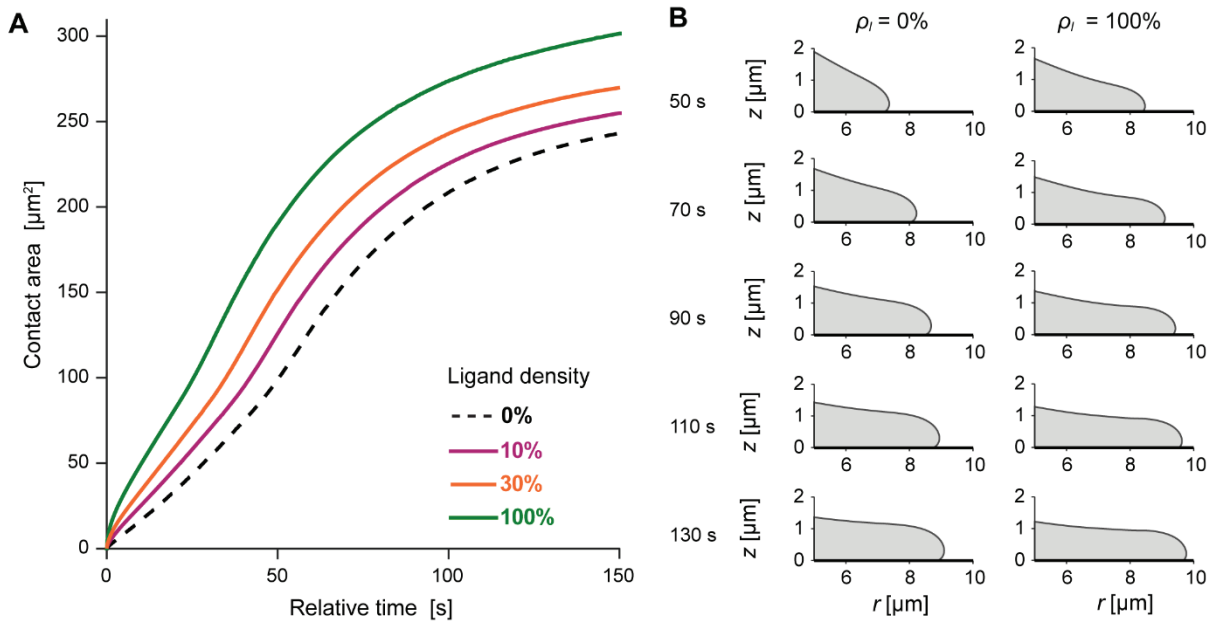


**Fig 6. Predictions of the protrusive zipper model with varying adhesion stress.** (A) Contact area increases faster and reaches higher values for higher ligand densities. The protrusion-only curve is shown for reference as a dashed line. (B) The leading edge of model cells spreading on $\rho_l = 0\%$ and $\rho_l = 100\%$ differ visibly at the sampled time points. On higher ligand density, both the extent of spreading and the dynamic contact angle increase.

Clearly, the predictions of the protrusive zipper model are in much better agreement with experimental observations than those of the Brownian zipper. A spreading cell morphology that is characterized by a forward-bulging leading lamella (Figs. 5-6) matches the cross-sectional profile of phagocytes engulfing large particles well [24, 34], in contrast to model cell shapes whose leading edge coincides with the perimeter of contact between the cell and substrate (Fig

413 3). The timing of spreading and sigmoidal shapes of the contact-area-versus-time curves
414 predicted by the protrusive zipper model (Fig 5-6) agree with experiments as well, and the time-
415 dependent increase in protrusion stress is consistent with a biphasic signaling response measured
416 during FcγR-mediated phagocytosis [35]. Furthermore, both the predicted spreading speeds as
417 well as the maximum contact areas are comparable to the respective values measured in
418 experiments, and the slight increase of the maximum contact area at higher adhesion strengths is
419 consistent with our measurements (Fig 6A). On the other hand, the predicted increase of the
420 spreading speeds on higher ligand densities (Fig 6A) differs from our experimental data (Fig 2).
421 Therefore, this model still somewhat overestimates the contribution of the adhesion stress to the
422 dynamics of phagocytic spreading. Nevertheless, of the two considered models only the
423 protrusive zipper model succeeds in capturing the essential dynamics of experimentally observed
424 phagocytic spreading, establishing that active cellular protrusion rather than passive cell-
425 substrate adhesion is the dominating driving force of this type of cellular motion.

426

## 427 Protrusive zipper model with discrete adhesion sites: best match 428 between experiments and theory

429 The previous sections presented continuum models of cell spreading, resulting in
430 predictions that overestimated the role of cell-substrate adhesion even in the case where short-
431 range adhesion plays only a secondary role. In reality, however, adhesive ligands encountered by
432 a spreading cell reside at discrete substrate locations rather than presenting a contiguous adhesive
433 film. A pioneering study that considered discrete adhesion sites not only predicted dramatic
434 qualitative differences compared to continuum models of adhesion but even concluded that,

435 depending on the lateral spacing of discrete cell-substrate cross-bridges, “there is little or no
436 tendency for the contact to spread unless the surfaces are forced together” [36]. These
437 considerations prompted us to design and examine a version of the protrusive zipper model in
438 which the model cell can only form new attachments to the substrate at prescribed locations (Fig
439 7, S5 Movie).

440

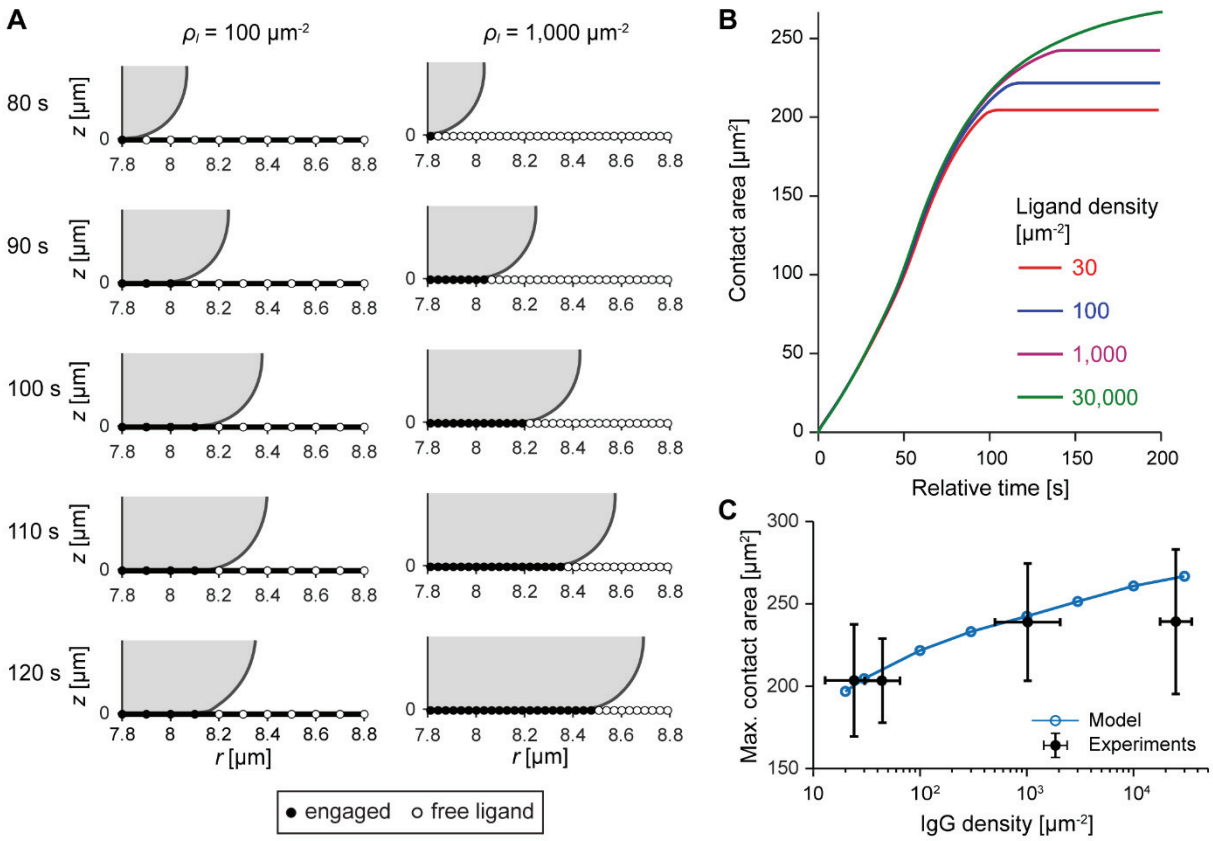


441 **Fig 7. Predictions of the protrusive zipper model with discrete adhesion sites.**
442 (A) Two time series (times shown at the left) of simulation snapshots illustrate how the
443 progression of the model cell’s leading edge is affected by the spacing of discrete adhesion sites.
444 Unoccupied binding sites are depicted by empty circles, whereas filled circles indicate that the
445 cell membrane is locally attached. (B) Contact area vs. time curves share similar slopes over

three orders of magnitude of ligand density, but plateau at different maximum contact areas. (C) The ligand-density-dependent increase in maximum contact area agrees well with experimental results obtained in frustrated phagocytosis experiments. Error bars indicate standard deviation.

In this model version, the spacing of adhesion sites is determined by the ligand density $\rho_l$ (the number of ligand molecules per μm$^2$), with the in-plane spacing given by $(\rho_l)^{-1/2}$. Furthermore, we introduce two additional rules to capture realistic aspects of cell spreading on discrete adhesion sites. First, we replace the continuous adhesion stress (Eq (6)) with the following concept of discrete bond formation. We consider a new bond as "formed" as soon as the distance between the next free ligand site and the closest point of the advancing cell membrane reaches a threshold distance $d_{thresh}$. As a consequence of such bonding, we place the cell surface into irreversible contact with this substrate site when carrying out computations at the next time step. The value of the threshold distance is determined by the magnitude of thermal membrane fluctuations. Assuming that the time scale of membrane fluctuations is generally smaller than our time step, we define $d_{thresh}$ to be the root mean square height $<h^2>^{½}$ of membrane fluctuations at equilibrium through [37]:

$$d_{thresh} = \sqrt{\langle h^2 \rangle} = \sqrt{\frac{k_B T}{4\pi\tau} \ln\left(1 + \frac{\tau A_{cell}}{\pi^2 \kappa_b}\right)} \tag{12}$$

where $k_B$ is Boltzmann's constant, $T$ is temperature, $A_{cell}$ is the cell surface area, and $\kappa_b$ is the membrane bending modulus. According to this rule, increased cortical tension $\tau$ suppresses membrane fluctuations, making it more difficult for the cell to form new adhesive connections at later time points.

467 Second, because it seems unlikely that persistent receptor-ligand contacts induce
468 signaling indefinitely, we also assume that the protrusion stress can diminish over time. This
469 assumption is supported by experimental data showing that actin polymerization does not
470 continue indefinitely during phagocytosis if the cell encounters an unopsonized region of the
471 target particle [18, 38, 39]. We implement this behavior by postulating a transient protrusion
472 stress that initially is triggered by fresh cell-substrate contact (occurring at time $t_{bind}$) and then
473 decays exponentially according to the relation:

474 $$\tilde{\sigma}_{prot} = \sigma_{prot} e^{-\frac{t - t_{bind}}{t_0}} \quad (13)$$

475 In this version of the model, $\sigma_{prot}$ in Eq (8) is replaced by $\tilde{\sigma}_{prot}$ defined in Eq (13).

476 To avoid possible bias due to the exact placement of discrete binding sites, we performed
477 each simulation multiple times, shifting all binding sites laterally by small increments without
478 changing their spacing. We then averaged the results of these individual simulations to predict
479 the cell-spreading behavior as a function of the chosen spacing—or density—of adhesion sites.

480 Overall, the predictions of this discrete protrusive zipper model (Fig 7) agree well with
481 those of the continuum model version. For instance, maximum cell-substrate contact areas
482 exhibit a similar dependence on the ligand density in both models. However, in this discrete
483 model, the sigmoidal contact-area-versus-time curves are aligned much more closely, reflecting
484 spreading speeds that hardly depend on the ligand density anymore (Fig 7B).

485 The behavior of model cells spreading on discrete adhesion sites agrees amazingly well
486 with that of real human neutrophils during frustrated phagocytosis. As in experiments, the
487 spreading speed remains remarkably consistent over a range of ligand densities spanning 3
488 orders of magnitude. Moreover, the moderate increase of the maximum contact area at higher

489 ligand densities successfully reproduces experimental observations (Fig 7C). These results
490 reinforce the conclusion that active cytoskeletal protrusion drives phagocytic spreading. They
491 also highlight that it can be important for realistic models of cell spreading on substrates coated
492 with specific adhesion molecules to account for the discrete distribution of these adhesion sites.

493

494 # Discussion

495 Quantitative understanding of the behavior of motile mammalian cells—from immune
496 cells to metastasizing cancer cells—is a prerequisite for transformative biomedical advances in
497 diagnosis, treatment, and therapy of many current and future health threats. Motile cells integrate
498 a complex variety of physical and chemical cues to carry out specific functions. Genuine
499 understanding of the underlying mechano-chemical processes not only requires an
500 interdisciplinary strategy but also integrative experimental/theoretical approaches. Translation of
501 mechanistic notions into mathematical models, and comparison of theoretical predictions with
502 experimental observations, often provides the strongest arguments for or against the validity of
503 biological hypotheses. Confidence in the predictive power of computer simulations requires that
504 the model assumptions be realistic and biologically plausible. Guided by this perspective, we
505 here examined fundamental biophysical mechanisms that potentially can facilitate spreading of
506 biological cells on a substrate.

507 Unpolarized cells usually begin spreading in a symmetric fashion [8, 40]. This stage is
508 often viewed as a passive process that is entirely driven by adhesion energy due to receptor-
509 ligand binding [8, 41]. An alternative class of models considers such spreading as dependent on
510 cytoskeletal activity [10, 14, 15]. In this study, we have developed a mechanical modeling

511 framework that allows us to establish whether frustrated phagocytosis, a specific form of
512 isotropic cell spreading, is primarily driven by adhesion (Brownian zipper model) or by
513 protrusive forces generated by the cell (protrusive zipper model). Our findings likely carry over
514 to other types of cell spreading inasmuch as key characteristics of adhesion and protrusion are
515 shared [42].

516 The incompatibility of our Brownian zipper simulations with experimental data
517 invalidates models of phagocytosis that treat neutrophil spreading as an adhesion-driven wetting
518 phenomenon [43]. Moreover, our findings invite a careful review of mathematical models of
519 other types of cell spreading that consider adhesion as the main driving force [8, 13]. A first
520 important prerequisite for the validity of such models is the use of realistic values of basic
521 mechanical parameters, such as the effective viscosity of the cell interior, the cortical tension,
522 and the adhesion energy density. For example, if the equilibrium cell-substrate contact areas
523 measured in our spreading experiments on low-to-moderate ligand densities were due to
524 adhesion, then the involved adhesion energies would have to be several orders of magnitude
525 higher than those estimated from our measurements of ligand density. Even receptor
526 accumulation in the contact region could not make up for this difference, because the smaller
527 number of available ligands limits the number of possible adhesion bonds. Furthermore, the
528 ability to simulate not only equilibrium situations but also the dynamical cell behavior, and to
529 leverage time-dependent experimental observations against the predictions of such models,
530 considerably raises confidence in a model's evaluation. As demonstrated in this study, such
531 comparison greatly benefits from the availability of experimental data obtained on substrates
532 presenting a large range of known densities of adhesive ligands.

533 It appears that adhesion-driven spreading is largely limited to situations where adhesion
534 is unusually strong, and where the cells—like red blood cells—or surrogate objects—like lipid
535 vesicles—are characterized by a low-viscosity interior and very low tension of their cortex or
536 membrane. Indeed, a recent mechanical modeling study found that Brownian membrane
537 fluctuations were only sufficient to drive very small amounts of cell spreading on a surface [44].
538 If there are cases in which motile mammalian cells spread predominantly due to adhesion, then
539 such spreading will likely occur on much longer timescales than considered here. Finally, it may
540 be possible that adhesion plays a more relevant role in the engulfment of very small particles
541 whose uptake does not require a significant expansion of the cell surface area. Irrespective of the
542 relevance of Brownian-zipper-type models in a particular practical situation, we note that the
543 excellent agreement of our theoretical treatment of purely adhesion-driven spreading with other
544 studies focusing on this form of motion [8, 13] strengthens confidence in our modeling approach
545 and its numerical implementation.

546 The only alternative mechanism by which cells can expand their region of contact with a
547 suitable substrate appears to be active, protrusion-dominated spreading. Many imaging studies
548 indeed have documented an increased density of F-actin at the protruding front of motile immune
549 cells [16, 45, 46], supporting the biological plausibility of the protrusive zipper concept.
550 Moreover, inhibition of actin polymerization with cytochalasin B or latrunculin A eliminates the
551 rapid phase of fibroblast spreading [10, 14, 47]. Similarly, chemical disruption of the actin
552 cytoskeleton generally inhibits phagocytosis by immune cells [28, 38]. We have previously
553 shown that extremely small concentrations of actin inhibitors actually can increase the size of
554 transient, chemotactic-like protrusions [28, 48]. However, the cortical tension was reduced in

555 such cases, and phagocytic spreading was not enhanced, highlighting the multiplicity of—likely
556 dichotomous—mechanical roles of F-actin during cell deformations.

557 Our simulations based on the protrusive zipper model not only reproduce the main
558 features of neutrophil spreading on IgG-coated substrates but, in the case of discrete adhesion
559 sites, they also agree very well with experimental data. We note that this agreement neither is
560 surprising, nor does it constitute solid proof of the validity of this model. The scarcity of
561 quantitative insights into the underlying mechanisms simply does not place sufficient constraints
562 on the design of computational models. Instead, our goal here was to explore what set of
563 minimalistic rules would need to be postulated to achieve a good match between theory and
564 experiment. The successful implementation of this approach allows us to propose likely
565 mechanistic details that can then provide guidance for future studies. Still, we are confident that
566 the protrusive zipper model paints a reasonably accurate picture of phagocytic spreading, not
567 only because of the elimination of the only alternative hypothesis, but also because our
568 semiempirical model is plausible, i.e., it does not contradict pertinent biophysical and biological
569 insights. For example, our implementation of the relationship between receptor-induced
570 signaling and the generation of protrusive force is consistent with the hitherto most successful
571 model of phagocytosis [24], as well as with previous measurements of the biphasic signaling
572 response from a macrophage-like cell line during Fcγ receptor-mediated phagocytosis [35].
573 Importantly, this implementation is independent of the exact mechanism by which intracellular
574 processes are translated into protrusive force; instead, it encompasses different mechanistic
575 notions such as the Brownian ratchet [49] and end-tracking motors [50].

576 An important outcome of our simulations of the protrusive zipper model is the difference
577 in predictions depending on whether we considered continuous or discrete cell-substrate

578 adhesion, in agreement with a previous theoretical study [36]. We are unaware of physiological
579 situations in which cell adhesion is not predominantly supported by specific receptor-ligand
580 bonds. Thus, the model version that is based on discrete binding sites is the more realistic version
581 of the protrusive zipper. Remarkably, it is also the version that yielded the best match between
582 theory and experimental observations. To achieve this agreement, we postulated that the
583 formation of new receptor-ligand bonds is coupled to the protrusion stress in a time-dependent
584 manner (Eq (13)), based on the assumption that receptor-induced signaling and subsequential
585 actin polymerization are not sustained indefinitely after a ligand activates the receptor. There are
586 multiple factors that could lead to this effective decay, such as the depletion of precursor
587 molecules needed for the production of signaling messengers (e.g. release of $IP_3$ will cease once
588 $PIP_2$ has been locally depleted [51]).

589 Perhaps the most important insight from the comparison of model versions based on
590 continuous versus discrete adhesion is that models based on continuous adhesion are likely to
591 misrepresent key aspects of the cell behavior, especially on lower ligand densities. For example,
592 such models cannot capture the possibility that too large ligand spacing may prevent the next
593 unbound receptor-ligand pair from approaching one another to within the distance at which they
594 are likely to form a bond. In our protrusive zipper model with discrete adhesion, variation of
595 substrate adhesivity by changing the density of adhesion sites primarily affects the maximum
596 cell-substrate contact area. This prediction agrees well with our experiments, unlike the
597 predictions by model versions that treat the ligand layer as a continuum.

598 The mechanisms governing isotropic cell spreading studied here are likely to also play a
599 crucial role in the directional motion of migrating cells. Many immune cells, for example, are
600 capable of executing both types of motion, as required during phagocytic spreading versus

601 chemotactic and other forms of migration. As revealed by our experiments and reproduced by
602 our discrete adhesion model, the rate of isotropic cell spreading is largely conserved on
603 substrates presenting a broad range of densities of adhesion sites. This finding exposes an
604 interesting difference to the prediction by models of migrating cells, i.e., that the crawling speed
605 of such cells has a maximum on substrates with intermediate adhesion strengths [52-54]. This
606 difference is a reminder that directional migration generally is a more complex type of motion
607 that involves, in addition to protrusion and adhesion, important mechanisms regulating
608 contraction and detachment of the rear of the migrating cell from the substrate. The positive
609 correlation between low-to-moderate ligand densities and the speed of motion predicted by
610 models of migrating cells can be attributed to either a direct scaling of protrusion with the
611 amount of adhesion [53], or a postulated increased actin retrograde flow at lower adhesion
612 strengths [52]. The predicted slowing of migrating cells at higher ligand densities is caused by an
613 effective frictional force due to the need to break stronger adhesive attachments at the cell's rear
614 [55, 56]. A noteworthy recent model of cell migration that decoupled friction from adhesive
615 attraction actually predicted faster movement for higher adhesion energies [41]. The excellent
616 agreement between our experiments and the protrusive zipper model suggests that the above
617 additional mechanisms included in models of migrating cells play at most a minor role in
618 isotropic phagocytic spreading. On the other hand, we believe that the main insights exposed by
619 our study provide important suggestions on how to treat the interplay between protrusion and
620 adhesion in models of migrating cells.

621

# Methods

## The perturbed Stokes equations

Assuming the cell interior can be approximated by a single, highly viscous, slow-moving Newtonian fluid, its motion obeys the Stokes equations for creeping flow with no body force, as given by Eq (2). Furthermore, for an incompressible fluid, the equation of continuity simplifies to the incompressibility condition (Eq (3)). Due to axial symmetry, there are three unknowns: $v_r$, $v_z$, and $p$, where $r$ and $z$ are cylindrical polar coordinates.

To solve this system of partial differential equations, we use the finite element method (FEM). Because directly solving the Stokes equations using FEM leads to numerical instabilities [57], we follow the procedure outlined by Drury and Dembo [29] to solve a perturbed form of the Stokes equations, in which the incompressibility condition (Eq (3)) is approximated as

$$\nabla \cdot (\mathbf{v} - \epsilon \nabla p) = 0 \tag{14}$$

In this form, the fluid is nearly incompressible, which allows us to avoid the well-known problems with using FEM for incompressible problems [57]. To accurately solve the Stokes equations, the value for $\epsilon$ must be sufficiently small. Specifically, we use the condition given in [29]:

$$\epsilon \leq \frac{h_{mesh}^2}{\mu} \tag{15}$$

where $h_{mesh}$ is the characteristic radius of a single quadrilateral element. We tested different values of $\epsilon$ in our models and found this condition to provide sufficient accuracy and convergence (Fig S5 in S6 Appendices).

Over the unbound portion of the cell, we specify Neumann boundary conditions, corresponding to a stress balance (Eq (4)). For the adherent cell surface, we specify Dirichlet boundary conditions, simply a no-slip condition in this case (Eq (9)). The pressure boundary condition is given by assuming the normal component of the pressure gradient goes to zero at the cell surface:

$$\nabla p \cdot \mathbf{n} = 0 \tag{16}$$

# Computational details

At each time step, we first compute values for the surface curvature of the cell. Local values of the angle of the normal $\phi$ are evaluated using cubic polynomial fits. We then calculate the boundary stresses using the relationships outlined in the main text. The integral for the effective adhesion stress (Eq (6)) is computed numerically as described in S6 Appendices. The values for tension and protrusion stress at each time step are evaluated using smoothed versions of the relationships given in Eq (1) and Eq (11) (see S6 Appendices for full forms).

To find the fluid velocity and pressure fields, we must simultaneously solve Eq (2) and Eq (14) for $v_r$, $v_z$, and $p$. We employ the strategy outlined in [29], which is an adaptation of the Uzawa method. Starting with an estimate for pressure $p_{est}$ given either by the previous time step or as a uniform distribution prior to spreading, we solve for fluid velocities by treating the pressure as known in Eq (2):

$$\mu \nabla^2 \mathbf{v} = \nabla p_{est} \tag{17}$$

We then treat the fluid velocities as known ($\mathbf{v}_{est}$) and solve an altered version of equation (14):

$$\frac{1}{\mu}(p - p_{est}) = \nabla \cdot \mathbf{v}_{est} - \nabla \cdot (\epsilon \nabla p) \tag{18}$$

The updated pressure is then inserted back into Eq (17) and the procedure is repeated until the following condition is met:

$$\frac{\max\left(\left|p - p_{est}\right|\right)}{\max\left(\left|p - p_{out}\right|\right)} \leq 10^{-6} \tag{19}$$

This generally occurs in less than 50 iterations.

The new cell boundary is then given by

$$\begin{aligned} r(t+\Delta t) &= r(t) + v_r \Delta t \\ z(t+\Delta t) &= z(t) + v_z \Delta t \end{aligned} \tag{20}$$

The value for $\Delta t$ was set relative to the Courant number for each iteration, such that fluid flow occurs over at most 10% of any individual element (S6 Appendices). In the continuum adhesion case (no discrete adhesion sites), the contact line is updated at each time step by computing the intersection between the cell boundary and the surface, then adding all points advected to $z \leq 0$ to the Dirichlet boundary condition (contact, no-slip) for the next time step. In the discrete adhesion model, contact is determined by the distance threshold computed from Eq (12). The contour is smoothed after each advection, and then small corrections are made to the cell contour to compensate for any deviations from constant volume due to smoothing and numerical error.

This model was implemented in MATLAB R2020b (MathWorks) and the full code is available at https://github.com/emmetfrancis/phagocyticSpreading. Individual simulations generally run within 1-3 hours on a personal computer.

681 # Acknowledgements

682 We thank Dr. Robert Guy from UC Davis Mathematics for many helpful conversations on
683 various iterations of our model and for assistance with the derivation found in S6 Appendices,
684 Appendix B. We also thank Dr. Marc Herant for fruitful discussions on computational modeling
685 of motile cells.

686

687 # References

688 1. Henry SJ, Crocker JC, Hammer DA. Ligand density elicits a phenotypic switch in human
689 neutrophils. Integr Biol (Camb). 2014;6(3):348-56. Epub 2014/02/01. doi:
690 10.1039/c3ib40225h. PubMed PMID: 24480897; PubMed Central PMCID:
691 PMCPMC5850933.
692 2. Hoang AN, Jones CN, Dimisko L, Hamza B, Martel J, Kojic N, et al. Measuring
693 neutrophil speed and directionality during chemotaxis, directly from a droplet of whole
694 blood. Technology (Singap World Sci). 2013;1(1):49. Epub 2014/05/09. doi:
695 10.1142/S2339547813500040. PubMed PMID: 24809064; PubMed Central PMCID:
696 PMCPMC4010229.
697 3. Ascione F, Vasaturo A, Caserta S, D'Esposito V, Formisano P, Guido S. Comparison
698 between fibroblast wound healing and cell random migration assays in vitro. Exp Cell
699 Res. 2016;347(1):123-32. doi: 10.1016/j.yexcr.2016.07.015. PubMed PMID:
700 WOS:000383217500013.

701 4. Czirok A. Endothelial cell motility, coordination and pattern formation during
702 vasculogenesis. Wiley Interdiscip Rev Syst Biol Med. 2013;5(5):587-602. Epub
703 2013/07/17. doi: 10.1002/wsbm.1233. PubMed PMID: 23857825; PubMed Central
704 PMCID: PMCPMC3737767.
705 5. Schneider L, Cammer M, Lehman J, Nielsen SK, Guerra CF, Veland IR, et al.
706 Directional cell migration and chemotaxis in wound healing response to PDGF-AA are
707 coordinated by the primary cilium in fibroblasts. Cell Physiol Biochem. 2010;25(2-
708 3):279-92. Epub 2010/01/30. doi: 10.1159/000276562. PubMed PMID: 20110689;
709 PubMed Central PMCID: PMCPMC2924811.
710 6. Morrissey MA, Williamson AP, Steinbach AM, Roberts EW, Kern N, Headley MB, et al.
711 Chimeric antigen receptors that trigger phagocytosis. Elife. 2018;7. doi: ARTN e36688
712 10.7554/eLife.36688. PubMed PMID: WOS:000435593500001.
713 7. Feng MY, Jiang W, Kim BYS, Zhang CC, Fu YX, Weissman IL. Phagocytosis
714 checkpoints as new targets for cancer immunotherapy. Nat Rev Cancer. 2019;19(10):568-
715 86. doi: 10.1038/s41568-019-0183-z. PubMed PMID: WOS:000492743400012.
716 8. Cuvelier D, Thery M, Chu YS, Dufour S, Thiery JP, Bornens M, et al. The universal
717 dynamics of cell spreading. Curr Biol. 2007;17(8):694-9. Epub 2007/03/24. doi:
718 10.1016/j.cub.2007.02.058. PubMed PMID: 17379524.
719 9. Dubin-Thaler BJ, Giannone G, Dobereiner HG, Sheetz MP. Nanometer analysis of cell
720 spreading on matrix-coated surfaces reveals two distinct cell states and STEPs. Biophys
721 J. 2004;86(3):1794-806. Epub 2004/03/03. doi: 10.1016/S0006-3495(04)74246-0.
722 PubMed PMID: 14990505; PubMed Central PMCID: PMCPMC1304013.

723 10. Xiong Y, Rangamani P, Fardin MA, Lipshtat A, Dubin-Thaler B, Rossier O, et al.
724 Mechanisms controlling cell size and shape during isotropic cell spreading. Biophys J.
725 2010;98(10):2136-46. Epub 2010/05/21. doi: 10.1016/j.bpj.2010.01.059. PubMed PMID:
726 20483321; PubMed Central PMCID: PMCPMC2872297.
727 11. Reinhart-King CA, Dembo M, Hammer DA. The dynamics and mechanics of endothelial
728 cell spreading. Biophys J. 2005;89(1):676-89. Epub 2005/04/26. doi:
729 10.1529/biophysj.104.054320. PubMed PMID: 15849250; PubMed Central PMCID:
730 PMCPMC1366566.
731 12. Carter SB. Haptotaxis and the mechanism of cell motility. Nature. 1967;213(5073):256-
732 60. Epub 1967/01/21. doi: 10.1038/213256a0. PubMed PMID: 6030602.
733 13. Etienne J, Duperray A. Initial dynamics of cell spreading are governed by dissipation in
734 the actin cortex. Biophys J. 2011;101(3):611-21. Epub 2011/08/03. doi:
735 10.1016/j.bpj.2011.06.030. PubMed PMID: 21806929; PubMed Central PMCID:
736 PMCPMC3145312.
737 14. Fardin MA, Rossier OM, Rangamani P, Avigan PD, Gauthier NC, Vonnegut W, et al.
738 Cell spreading as a hydrodynamic process. Soft Matter. 2010;6(19):4788-99. doi:
739 10.1039/c0sm00252f. PubMed PMID: WOS:000282008300022.
740 15. Herant M, Dembo M. An integrative toy model of cell flattening, spreading, and ruffling.
741 Biorheology. 2015;52(5-6):405-14. Epub 2015/11/26. doi: 10.3233/BIR-14042. PubMed
742 PMID: 26600264.
743 16. Kovari DT, Wei W, Chang P, Toro JS, Beach RF, Chambers D, et al. Frustrated
744 Phagocytic Spreading of J774A-1 Macrophages Ends in Myosin II-Dependent
745 Contraction. Biophys J. 2016;111(12):2698-710. Epub 2016/12/22. doi:

746 10.1016/j.bpj.2016.11.009. PubMed PMID: 28002746; PubMed Central PMCID:
747 PMCPMC5194617.
748 17. Cannon GJ, Swanson JA. The macrophage capacity for phagocytosis. J Cell Sci.
749 1992;101 ( Pt 4):907-13. Epub 1992/04/01. PubMed PMID: 1527185.
750 18. Heinrich V. Controlled One-on-One Encounters between Immune Cells and Microbes
751 Reveal Mechanisms of Phagocytosis. Biophys J. 2015;109(3):469-76. Epub 2015/08/06.
752 doi: 10.1016/j.bpj.2015.06.042. PubMed PMID: 26244729; PubMed Central PMCID:
753 PMCPMC4572503.
754 19. Francis EA, Xiao H, Teng LH, Heinrich V. Mechanisms of frustrated phagocytic
755 spreading of human neutrophils on antibody-coated surfaces. 2022;
756 BIORXIV/2022/481104.
757 20. Evans E, Yeung A. Apparent viscosity and cortical tension of blood granulocytes
758 determined by micropipet aspiration. Biophys J. 1989;56(1):151-60. Epub 1989/07/01.
759 doi: 10.1016/S0006-3495(89)82660-8. PubMed PMID: 2752085; PubMed Central
760 PMCID: PMCPMC1280460.
761 21. Tran-Son-Tay R, Needham D, Yeung A, Hochmuth RM. Time-dependent recovery of
762 passive neutrophils after large deformation. Biophys J. 1991;60(4):856-66. Epub
763 1991/10/01. doi: 10.1016/S0006-3495(91)82119-1. PubMed PMID: 1742456; PubMed
764 Central PMCID: PMCPMC1260136.
765 22. Yeung A, Evans E. Cortical shell-liquid core model for passive flow of liquid-like
766 spherical cells into micropipets. Biophys J. 1989;56(1):139-49. Epub 1989/07/01. doi:
767 10.1016/S0006-3495(89)82659-1. PubMed PMID: 2752083; PubMed Central PMCID:
768 PMCPMC1280459.

769 23. Herant M, Marganski WA, Dembo M. The mechanics of neutrophils: synthetic modeling
770 of three experiments. Biophys J. 2003;84(5):3389-413. Epub 2003/04/30. doi:
771 10.1016/s0006-3495(03)70062-9. PubMed PMID: 12719267; PubMed Central PMCID:
772 PMCPMC1302898.
773 24. Herant M, Heinrich V, Dembo M. Mechanics of neutrophil phagocytosis: experiments
774 and quantitative models. J Cell Sci. 2006;119(Pt 9):1903-13. Epub 2006/04/26. doi:
775 10.1242/jcs.02876. PubMed PMID: 16636075.
776 25. Herant M, Lee CY, Dembo M, Heinrich V. Protrusive push versus enveloping embrace:
777 computational model of phagocytosis predicts key regulatory role of cytoskeletal
778 membrane anchors. PLoS Comput Biol. 2011;7(1):e1001068. doi:
779 10.1371/journal.pcbi.1001068. PubMed PMID: 21298079; PubMed Central PMCID:
780 PMCPMC3029235.
781 26. Zak A, Merino-Cortes SV, Sadoun A, Mustapha F, Babataheri A, Dogniaux S, et al.
782 Rapid viscoelastic changes are a hallmark of early leukocyte activation. Biophys J. 2021.
783 Epub 2021/03/18. doi: 10.1016/j.bpj.2021.02.042. PubMed PMID: 33730552.
784 27. Herant M, Heinrich V, Dembo M. Mechanics of neutrophil phagocytosis: behavior of the
785 cortical tension. J Cell Sci. 2005;118(Pt 9):1789-97. Epub 2005/04/14. doi:
786 10.1242/jcs.02275. PubMed PMID: 15827090.
787 28. Lee CY, Herant M, Heinrich V. Target-specific mechanics of phagocytosis: protrusive
788 neutrophil response to zymosan differs from the uptake of antibody-tagged pathogens. J
789 Cell Sci. 2011;124(Pt 7):1106-14. Epub 2011/03/10. doi: 10.1242/jcs.078592. PubMed
790 PMID: 21385838; PubMed Central PMCID: PMCPMC3056606.

791 29. Drury JL, Dembo M. Hydrodynamics of micropipette aspiration. Biophys J. 1999;76(1 Pt
792 1):110-28. Epub 1999/01/06. doi: 10.1016/S0006-3495(99)77183-3. PubMed PMID:
793 9876128; PubMed Central PMCID: PMCPMC1302505.
794 30. Maenaka K, van der Merwe PA, Stuart DI, Jones EY, Sondermann P. The human low
795 affinity Fcgamma receptors IIa, IIb, and III bind IgG with fast kinetics and distinct
796 thermodynamic properties. J Biol Chem. 2001;276(48):44898-904. Epub 2001/09/07.
797 doi: 10.1074/jbc.M106819200. PubMed PMID: 11544262.
798 31. Bonn D, Eggers J, Indekeu J, Meunier J, Rolley E. Wetting and spreading. Rev Mod
799 Phys. 2009;81(2):739-805. doi: 10.1103/RevModPhys.81.739. PubMed PMID:
800 WOS:000267197500008.
801 32. Marcy Y, Prost J, Carlier MF, Sykes C. Forces generated during actin-based propulsion:
802 a direct measurement by micromanipulation. Proc Natl Acad Sci U S A.
803 2004;101(16):5992-7. Epub 2004/04/14. doi: 10.1073/pnas.0307704101. PubMed PMID:
804 15079054; PubMed Central PMCID: PMCPMC395911.
805 33. Parekh SH, Chaudhuri O, Theriot JA, Fletcher DA. Loading history determines the
806 velocity of actin-network growth. Nat Cell Biol. 2005;7(12):1219-23. Epub 2005/11/22.
807 doi: 10.1038/ncb1336. PubMed PMID: 16299496.
808 34. Lee C-Y, Thompson III GR, Hastey CJ, Hodge GC, Lunetta JM, Pappagianis D, et al.
809 *Coccidioides* Endospores and Spherules Draw Strong Chemotactic, Adhesive, and
810 Phagocytic Responses by Individual Human Neutrophils. PLoS ONE.
811 2015;10(6):e0129522. doi: 10.1371/journal.pone.0129522.
812 35. Zhang Y, Hoppe AD, Swanson JA. Coordination of Fc receptor signaling regulates
813 cellular commitment to phagocytosis. Proc Natl Acad Sci U S A. 2010;107(45):19332-7.

814 Epub 2010/10/27. doi: 10.1073/pnas.1008248107. PubMed PMID: 20974965; PubMed
815 Central PMCID: PMCPMC2984174.
816 36. Evans EA. Detailed mechanics of membrane-membrane adhesion and separation. II.
817 Discrete kinetically trapped molecular cross-bridges. Biophys J. 1985;48(1):185-92.
818 Epub 1985/07/01. doi: 10.1016/S0006-3495(85)83771-1. PubMed PMID: 4016208;
819 PubMed Central PMCID: PMCPMC1329388.
820 37. Helfrich W, Servuss RM. Undulations, Steric Interaction and Cohesion of Fluid
821 Membranes. Nuovo Cimento D. 1984;3(1):137-51. doi: Doi 10.1007/Bf02452208.
822 PubMed PMID: WOS:A1984SF44800012.
823 38. van Zon JS, Tzircotis G, Caron E, Howard M. A mechanical bottleneck explains the
824 variation in cup growth during FcgammaR phagocytosis. Mol Syst Biol. 2009;5:298.
825 Epub 2009/08/20. doi: 10.1038/msb.2009.59. PubMed PMID: 19690567; PubMed
826 Central PMCID: PMCPMC2736656.
827 39. Griffin FM, Jr., Griffin JA, Leider JE, Silverstein SC. Studies on the mechanism of
828 phagocytosis. I. Requirements for circumferential attachment of particle-bound ligands to
829 specific receptors on the macrophage plasma membrane. J Exp Med. 1975;142(5):1263-
830 82. Epub 1975/11/11. doi: 10.1084/jem.142.5.1263. PubMed PMID: 1194852; PubMed
831 Central PMCID: PMCPMC2189973.
832 40. McGrath JL. Cell spreading: the power to simplify. Curr Biol. 2007;17(10):R357-8. Epub
833 2007/05/16. doi: 10.1016/j.cub.2007.03.057. PubMed PMID: 17502086.
834 41. Cao Y, Karmakar R, Ghabache E, Gutierrez E, Zhao Y, Groisman A, et al. Cell motility
835 dependence on adhesive wetting. Soft Matter. 2019;15(9):2043-50. Epub 2019/02/07.
836 doi: 10.1039/c8sm01832d. PubMed PMID: 30724956.

837 42. Cougoule C, Wiedemann A, Lim J, Caron E. Phagocytosis, an alternative model system
838 for the study of cell adhesion. Semin Cell Dev Biol. 2004;15(6):679-89. Epub
839 2004/11/25. doi: 10.1016/j.semcdb.2004.09.001. PubMed PMID: 15561587.
840 43. Tollis S, Dart AE, Tzircotis G, Endres RG. The zipper mechanism in phagocytosis:
841 energetic requirements and variability in phagocytic cup shape. BMC Syst Biol.
842 2010;4:149. Epub 2010/11/10. doi: 10.1186/1752-0509-4-149. PubMed PMID:
843 21059234; PubMed Central PMCID: PMCPMC2991294.
844 44. DiNapoli KT, Robinson DN, Iglesias PA. A mesoscale mechanical model of cellular
845 interactions. Biophys J. 2021;120(22):4905-17. Epub 2021/10/24. doi:
846 10.1016/j.bpj.2021.10.021. PubMed PMID: 34687718; PubMed Central PMCID:
847 PMCPMC8633826.
848 45. Nelsen E, Hobson CM, Kern ME, Hsiao JP, O'Brien Iii ET, Watanabe T, et al. Combined
849 Atomic Force Microscope and Volumetric Light Sheet System for Correlative Force and
850 Fluorescence Mechanobiology Studies. Sci Rep. 2020;10(1):8133. Epub 2020/05/20. doi:
851 10.1038/s41598-020-65205-8. PubMed PMID: 32424215; PubMed Central PMCID:
852 PMCPMC7234992.
853 46. Fritz-Laylin LK, Riel-Mehan M, Chen BC, Lord SJ, Goddard TD, Ferrin TE, et al. Actin-
854 based protrusions of migrating neutrophils are intrinsically lamellar and facilitate
855 direction changes. Elife. 2017;6. Epub 2017/09/28. doi: 10.7554/eLife.26990. PubMed
856 PMID: 28948912; PubMed Central PMCID: PMCPMC5614560.
857 47. Dubin-Thaler BJ, Hofman JM, Cai Y, Xenias H, Spielman I, Shneidman AV, et al.
858 Quantification of cell edge velocities and traction forces reveals distinct motility modules
859 during cell spreading. PLoS One. 2008;3(11):e3735. Epub 2008/11/18. doi:

860 10.1371/journal.pone.0003735. PubMed PMID: 19011687; PubMed Central PMCID:
861 PMCPMC2581916.
862 48. Heinrich V, Lee C-Y. Blurred line between chemotactic chase and phagocytic
863 consumption: an immunophysical single-cell perspective. Journal of Cell Science.
864 2011;124(18):3041-51. doi: 10.1242/jcs.086413.
865 49. Mogilner A, Oster G. Cell motility driven by actin polymerization. Biophys J.
866 1996;71(6):3030-45. Epub 1996/12/01. doi: 10.1016/S0006-3495(96)79496-1. PubMed
867 PMID: 8968574; PubMed Central PMCID: PMCPMC1233792.
868 50. Dickinson RB, Caro L, Purich DL. Force generation by cytoskeletal filament end-
869 tracking proteins. Biophys J. 2004;87(4):2838-54. Epub 2004/09/30. doi:
870 10.1529/biophysj.104.045211. PubMed PMID: 15454475; PubMed Central PMCID:
871 PMCPMC1304702.
872 51. Flannagan RS, Jaumouille V, Grinstein S. The cell biology of phagocytosis. Annu Rev
873 Pathol. 2012;7:61-98. Epub 2011/09/14. doi: 10.1146/annurev-pathol-011811-132445.
874 PubMed PMID: 21910624.
875 52. Barnhart EL, Lee KC, Keren K, Mogilner A, Theriot JA. An adhesion-dependent switch
876 between mechanisms that determine motile cell shape. PLoS Biol. 2011;9(5):e1001059.
877 Epub 2011/05/12. doi: 10.1371/journal.pbio.1001059. PubMed PMID: 21559321;
878 PubMed Central PMCID: PMCPMC3086868.
879 53. Ziebert F, Aranson IS. Effects of adhesion dynamics and substrate compliance on the
880 shape and motility of crawling cells. PLoS One. 2013;8(5):e64511. Epub 2013/06/07.
881 doi: 10.1371/journal.pone.0064511. PubMed PMID: 23741334; PubMed Central
882 PMCID: PMCPMC3669322.

54. Copos CA, Walcott S, Del Alamo JC, Bastounis E, Mogilner A, Guy RD. Mechanosensitive Adhesion Explains Stepping Motility in Amoeboid Cells. Biophys J. 2017;112(12):2672-82. Epub 2017/06/22. doi: 10.1016/j.bpj.2017.04.033. PubMed PMID: 28636923; PubMed Central PMCID: PMCPMC5478966.

55. Shao D, Levine H, Rappel WJ. Coupling actin flow, adhesion, and morphology in a computational cell motility model. Proc Natl Acad Sci U S A. 2012;109(18):6851-6. Epub 2012/04/12. doi: 10.1073/pnas.1203252109. PubMed PMID: 22493219; PubMed Central PMCID: PMCPMC3344950.

56. Kuusela E, Alt W. Continuum model of cell adhesion and migration. J Math Biol. 2009;58(1-2):135-61. Epub 2008/05/20. doi: 10.1007/s00285-008-0179-x. PubMed PMID: 18488227.

57. Hughes TJR. The Finite Element Method: Linear Static and Dynamic Finite Element Analysis: Dover; 2000.

# Supporting Information

**S1 Movie. Simulations of purely adhesive cell spreading ("Brownian zipper") on substrates presenting different densities of adhesion sites.** This sequence of animations shows side views of model cells spreading on adhesive substrates coated with relative ligand densities ($\rho_l$) of 1%, 3%, 10%, 30%, and 100% for 400 s in the absence of protrusion stress.

**S2 Movie. Simulation of purely protrusion-driven cell spreading.** This animation shows a side view of a model cell spreading on a flat substrate for 200 s. The cell motion is assumed to be driven exclusively by active cytoskeletal protrusion at a maximum protrusion stress of $\sigma_{prot,max}$ =

905 3.5 kPa. Cell-substrate contact, once established, is assumed to be permanent. All other
906 contributions of adhesive cell-substrate interactions to spreading are neglected.

907 **S3 Movie. Effect of the range of action of the protrusion stress on purely protrusion-driven**
908 **cell spreading.** This sequence of simulations shows side views of model cells spreading in the
909 absence of adhesion stress for 200 s. Increasing the range $s_0$ over which cytoskeletal protrusion
910 actively pushes the cellular pseudopod outwards (given in terms of the arc length of the free cell
911 contour, measured from the point of substrate contact) results in thicker pseudopods. In this
912 sequence, $s_0$ = 0.4 μm, 1.2 μm, and 2.0 μm, respectively. In all examples, $\sigma_{prot,max} \times s_0$ = 2.8
913 mN/m.

914 **S4 Movie. Minor role of cell-substrate adhesion stress in protrusion-dominated cell**
915 **spreading ("protrusive zipper").** This sequence of simulations compares magnified views of
916 purely protrusion-driven spreading (adhesion stress $\rho_l$ = 0%) with protrusion-driven spreading in
917 the presence of moderate and strong adhesion stress ($\rho_l$ = 10% and 100%, respectively). In all
918 examples, $\sigma_{prot,max}$ = 3.5 kPa.

919 **S5 Movie. Protrusive zipper simulations with discrete adhesion sites.** This sequence of
920 simulations shows a magnified view of protrusion-driven spreading ($\sigma_{prot,max}$ = 3.5 kPa) on
921 substrates presenting different densities of discrete adhesion sites ($\rho_l$ = 30 μm$^{-2}$, 100 μm$^{-2}$, 1,000
922 μm$^{-2}$, and 10,000 μm$^{-2}$). Open circles denote free adhesive binding sites, and filled circles depict
923 sites with engaged ligand.

924 **S6 Appendices. Derivation of important relationships and summary of numerical testing.**
925 (A) Adhesion stress calculation. (B) Derivation of a power law for contact area growth in passive

spreading. (C) Development of $C^1$ versions of tension and protrusion stress relations. (D) Details of finite element implementation. (E) Summary of numerical testing.

**S7 Table. Summary of modeling parameters, with supporting references.**

# S6 Appendices

## Appendix A. Adhesion stress calculation

To compute the adhesion stress, we consider a potential acting between an adhesion molecule and a receptor in the cell membrane. Here, we use a 6-3 potential:

$$u_{adh}(D) = u_0\left[\left(\frac{D_0}{D}\right)^6 - 2\left(\frac{D_0}{D}\right)^3\right] \tag{S1}$$

where $D_0$ is the distance associated with the energy minimum and $u_0$ sets the magnitude of the binding energy. The force due to this single interaction is

$$f_{adh}(D) = -\frac{du_{adh}(D)}{dD} = f_0\left[\left(\frac{D_0}{D}\right)^7 - \left(\frac{D_0}{D}\right)^4\right] \tag{S2}$$

where $f_0 = 6u_0/D_0$. As $D_0$ is the location of the energy minimum, we also see that $f_{adh}(D_0) = 0$. We use $D_0 = 50$ nm in our simulations. Realistically, one might expect this distance to be much smaller (molecular scale), but the longer range here effectively includes membrane fluctuations and filopodia, and effectively serves as an upper limit. Adhesion potentials with a range of tens to hundreds of nanometers are common when modeling cells and vesicles at the mesoscopic scale [1, 2].

To solve for the overall adhesion stress, we must integrate over the ligand-coated surface (surface coordinates $[r, \theta]$ ) and the region of membrane being considered (surface coordinates $[s, \psi]$ ) (Fig S1A).

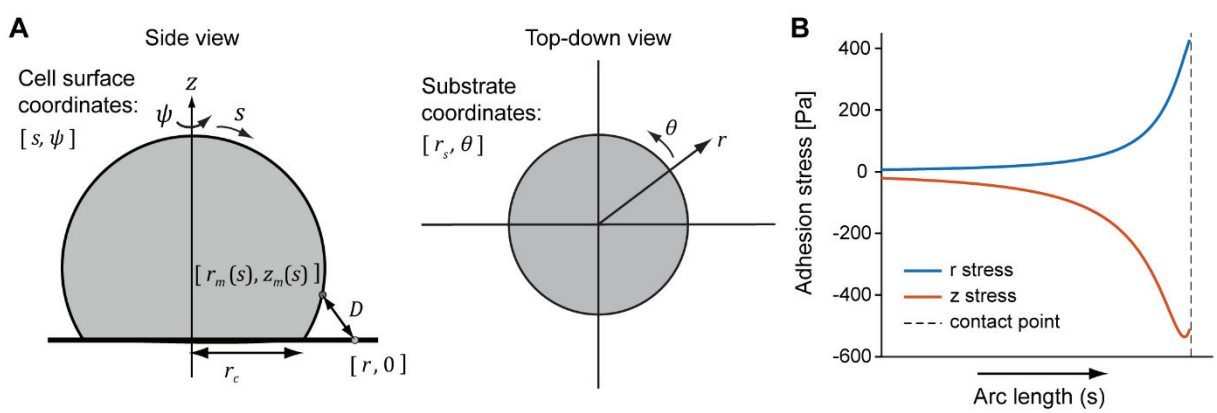


**Fig S1. Adhesion force calculation.**
(A) The cell geometry is depicted from the side, as well as from the top, including definitions of coordinates used in the text. (B) Adhesion stress components are plotted as a function of arc length $s$ for the cell shape shown in part A given a relative ligand density of 10%.

The individual interaction forces must be specified as vectors, that is

$$\mathbf{f}_{single} = f_0 \left[ \left( \frac{D_0}{D} \right)^7 - \left( \frac{D_0}{D} \right)^4 \right] \mathbf{f}_{unit} \tag{S3}$$

The distance between a point on the membrane and a point on the surface is given by

$$D(r, \theta, s, \psi) = \sqrt{(r_m \cos\psi - r\cos\theta)^2 + (r_m \sin\psi - r\sin\theta)^2 + z_m^2} \tag{S4}$$

Note that the distance $z_m$ is adjusted from the $z$ coordinate used elsewhere so that the surface $z = 0$ corresponds to the zero-force distance $D_0$, i.e. $z_m = z + D_0$.

The direction of the force is expressed by a unit vector (we only calculate the $r$ and $z$ components, as the angular component cancels out due to symmetry)

$$\mathbf{f}_{unit} = \frac{1}{D} \begin{bmatrix} r_m \cos\psi - r\cos\theta \\ z_m \end{bmatrix} \tag{S5}$$

Considering a region of the cell membrane extending from $s = s_{cur} - l$ to $s = s_{cur} + l$ along the arc length and from $\psi = -\Delta\psi/2$ to $\psi = \Delta\psi/2$ in the angular direction, we compute the pairwise force by the total integral

$$\mathbf{f}_{adh} = \int_{-\Delta\psi/2}^{\Delta\psi/2} \int_{s_{cur}-\frac{l}{2}}^{s_{cur}+\frac{l}{2}} \left( \int_0^{2\pi} \int_{r_c}^{\infty} \mathbf{f}_{single} \rho_l r dr d\theta \right) \rho_R r_m ds d\psi \tag{S6}$$

where $\rho_l$ is the ligand density on the substrate and $\rho_R$ is the receptor density on the cell membrane. In practice, we lump $f_0$ and $\rho_R$ into a single parameter $\sigma_0 = f_0 \rho_R$, which effectively serves as a force per unit area of cell membrane.

The stress per unit area of membrane is given by

$$\boldsymbol{\sigma}_{adh} = \frac{\mathbf{f}_{adh}}{\int_{-\Delta\psi/2}^{\Delta\psi/2} \int_{s_{cur}-\frac{l}{2}}^{s_{cur}+\frac{l}{2}} r_m ds d\psi} \tag{S7}$$

In the limit $l\Delta\psi \to 0$, we obtain the final expression, as given in the main text

$$\boldsymbol{\sigma}_{adh} = \sigma_0 \rho_l \int_0^{2\pi} \int_{r_{edge}}^{\infty} \mathbf{f}_{unit} \left[ \left( \frac{D_0}{D} \right)^7 - \left( \frac{D_0}{D} \right)^4 \right] r dr d\theta \tag{S8}$$

Due to the embedded trigonometric functions, this integral is not readily carried out analytically unless we use a small angle estimate for $\theta$, which will not hold in general. Therefore, we evaluate it numerically in MATLAB by performing trapezoidal integration twice, using log-spaced meshes for both $r$ and $\theta$. This achieves essentially the same results as integration with MATLAB built-in functions, but computation time is reduced well over 10-fold.

An example of the adhesion stress components computed as a function of arc length $s$ along the cell contour shown in Fig S1A for $\rho_l = 10\%$ is shown in Fig S1B.

In practice, we modify the adhesion strength in simulations by varying the multiplicative factor $\sigma_0\rho_l$, but we cannot directly extract the ligand density $\rho_l$. However, as described in the main text, we can infer the adhesion energy per unit area $\gamma$ from the equilibrium contact area $A_c$ using simple geometry, conservation of volume, and the Young-Dupre equation. Using these estimated values of adhesion energy $\gamma(A_c)$ and the typical binding energy of a low affinity Fcγ receptor to IgG ($E_{bind} \approx 6 \times 10^{-20}$ J [3]), we can estimate the corresponding IgG density $\rho_{IgG,est}$

$$\rho_{IgG,est} = \frac{\gamma(A_c)}{E_{bind}} \tag{S9}$$

We perform a linear fit between $\rho_{IgG,est}$ and the relative adhesion strength $\rho_l / \rho_{l,max}$ to compute the effective IgG densities tested in our Brownian Zipper model (Fig S2B). From this fit, we find that $\rho_l = 10\%$ roughly corresponds to $\rho_{IgG,est} = 1{,}000$ μm$^{-2}$.

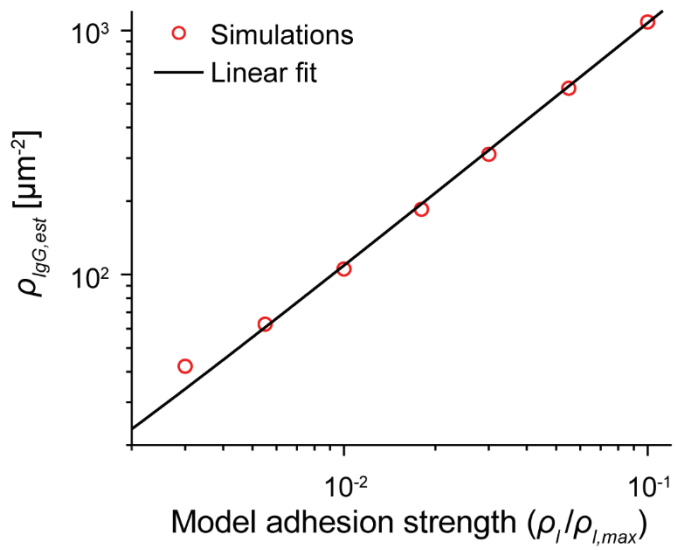


**Fig S2. Relationship between estimated IgG density and model adhesion strength**.
A linear fit relates model adhesion strength to IgG density based on the equilibrium contact areas we obtain from simulations.

## Appendix B. Derivation of a power law for contact area growth in passive spreading

To develop an approximate analytical prediction of the functional dependence of the contact area on time, we start from the overall energy balance for our passive model cell spreading on a flat surface with adhesion energy density $\gamma$, directly analogous to the energy balance in the spreading of a viscous droplet [4]. After canceling a factor of 2π, this yields

$$\frac{\gamma}{2}\frac{\partial}{\partial t}(r_c^2) = 2\mu \iint e_{ij}e_{ij} r\mathrm{d}r\mathrm{d}z + \frac{\partial}{\partial t}\left(\tau \int r ds\right) + \frac{\partial}{\partial t}\left(\iint p r\mathrm{d}r\mathrm{d}z\right) \tag{S10}$$

where $r_c$ is the cell contact radius, $\mu$ is the effective cell viscosity, $e_{ij}$ are the components of the rate-of-strain tensor, $\tau$ is the cortical tension, and $p$ is the pressure inside the cell. The left-hand side corresponds to energy gain due to cell-surface adhesion. The first term on the right-hand side is the viscous dissipation rate [5], the second term is the work required to deform the cortex, and the third is the change in energy due to changes in pressure and/or volume. In our simulations volume is kept constant, and any energy required for pressure changes is much lower than for changes of the surface area or tension; therefore, we neglect the last term of Eq S10 in the following analysis.

To estimate the remaining terms in the energy balance, we assume that the passively spreading cell adopts the shape of a spherical cap with contact radius $r_c$, radius of curvature $R_{cell}$, and a constant volume (Fig S3A). This geometry defines the contact angle as:

$$\sin\theta_c = \frac{r_c}{R_{cell}} \tag{S11}$$

We focus this analysis on initial contact area growth, during which the contact angle is small and we can treat $R_{cell}$ as a constant. Based on this geometry and features of the calculated flow profile (Fig S3A inset), we estimate the viscous dissipation rate and work required to deform the cortex as follows.

We first expand the dissipation term to include all non-zero components of the rate-of-strain tensor (all derivatives with respect to the polar angle are zero given axial symmetry):

$$\Pi = \mu \iint \left[2\left(\frac{\partial v_r}{\partial r}\right)^2 + 2\left(\frac{v_r}{r}\right)^2 + 2\left(\frac{\partial v_z}{\partial z}\right)^2 + \left(\frac{\partial v_r}{\partial z} + \frac{\partial v_z}{\partial r}\right)^2\right] r\mathrm{d}r\mathrm{d}z \tag{S12}$$

The main effect of the adhesion force is to "pull down" the membrane onto the flat surface; that is, the $z$-component of the adhesion stress generally dominates (Fig 1B). Accordingly, we expect $v_z$ to dominate over $v_r$ in the portion of the cell closest to the substrate, which we do in fact see in our calculations (Fig S3A inset). Furthermore, due to incompressibility, we know

$$\frac{v_r}{r} + \frac{\partial v_r}{\partial r} + \frac{\partial v_z}{\partial z} = 0 \tag{S13}$$

Therefore, if the contributions of $v_r$ are small, $\partial v_z/\partial z$ must also be small, and we are left with:

$$\Pi \approx \mu \iint \left(\frac{\partial v_z}{\partial r}\right)^2 r dr dz \tag{S14}$$

As a test geometry for points near the surface, we consider a wedge shape, as shown in Fig S3B. The exact functional form of $v_z$ within this wedge cannot be readily inferred *a priori*. Instead, we identify characteristic length scales to estimate the velocity gradient. We expect the $z$-velocity to be highest close to the surface, that is, within the length scale set by the adhesion potential ($D_0$). For this region, the associated distance in the $r$ direction $\Delta r$ (Fig S3B) is given by

$$\Delta r = \frac{D_0}{\tan\theta_c} \approx \frac{D_0 R_{cell}}{r_c} \tag{S15}$$

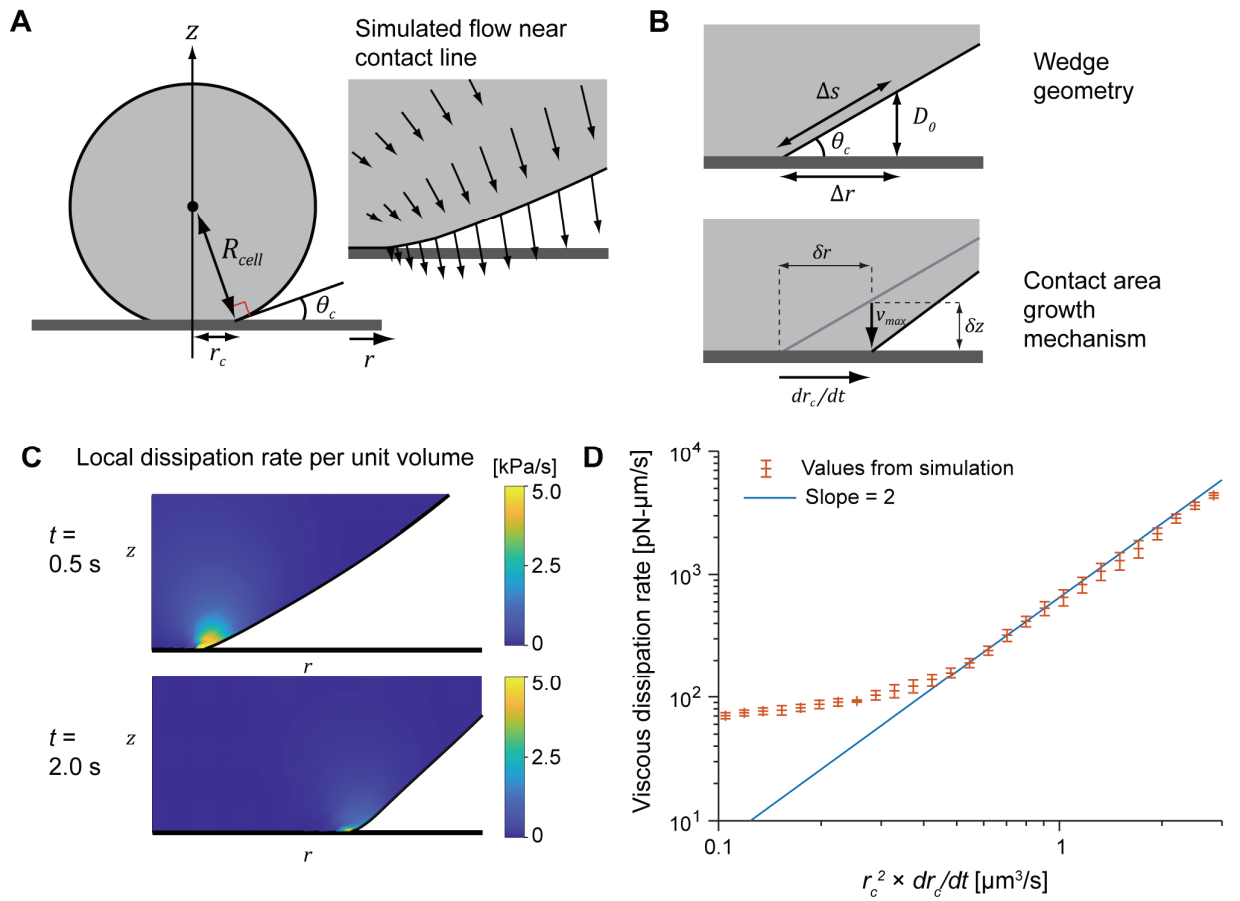


**Fig S3.** Energy balance calculations.
(A) Geometry of a spreading droplet during early spreading. The inset illustrates fluid velocities (arrows) at the boundary near the contact line as predicted by a typical Brownian zipper simulation. (B) Simplified geometry of a wedge used to represent a spreading droplet. The top panel defines variable used in the text. The bottom panel illustrates the manner of contact area growth implemented in our model. (C) Local dissipation per unit volume at the contact line for two early time points as computed by a Brownian zipper simulation at a ligand density of 10%. The dissipation is tightly confined to the point of contact. (D) Total viscous dissipation rate was directly computed using linear shape functions and plotted against $r_c^2 \times dr_c/dt$ on a log-log axis. Simulated values were binned and averaged for each interval on the x-axis. Error bars indicate standard deviation of binned data.

Before estimating the velocity gradient, we relate $v_z$ to the rate of contact area growth, $dr_c/dt$. Because there is no slip at the contact line itself, the only way for the contact area to increase is for nonadherent membrane to approach and touch the surface past the contact line. We consider a sample point close to the surface at which the membrane moves at maximum velocity $v_{max}$ in the negative $z$ direction (Fig S3B). If this point moves down from a distance $\delta z$ from the surface, then the contact line moves outward by a distance of $\delta r$ in the $r$-direction (Fig S3B), given by

$$\delta r = \frac{\delta z}{\tan \theta_c} \tag{S16}$$

In terms of velocities, this yields

$$\frac{dr_c}{dt} = \frac{v_{max}}{\tan \theta_c} \approx \frac{v_{max} R_{cell}}{r_c} \tag{S17}$$

Combining Eqs S15 and S17 and assuming the velocity gradient is highest in the direction tangent to the membrane, we approximate the sought velocity gradient:

$$\frac{\partial v_z}{\partial r} \approx \frac{v_{max}}{\Delta r} = \frac{r_c^2}{R_{cell}^2 D_0} \frac{dr_c}{dt} \tag{S18}$$

We insert these estimates into the dissipation term (Eq S14) and integrate over the wedge:

$$\Pi \approx \mu \left( \frac{r_c^2}{R_{cell}^2 r_0} \frac{dr_c}{dt} \right)^2 \int_{r_c}^{r_c+\Delta r} \int_{D_0 \frac{(r-r_c)}{\Delta r}}^{D_0} r dz dr \tag{S19}$$

$$= \mu \left( \frac{r_c^2}{R_{cell}^2 D_0} \frac{dr_c}{dt} \right)^2 \frac{D_0 \Delta r}{6} (3r_c + \Delta r)$$

Inserting the definition of $\Delta r$ from Eq S15 and assuming $\Delta r << 3r_c$, we find

$$\Pi \approx \Pi_0 r_c^4 \left( \frac{dr_c}{dt} \right)^2 \tag{S20}$$

where $\Pi_0 = \mu/(2R_{cell}^3)$. We verify the validity of this relationship by comparing it to numerically computed dissipation rates obtained in Brownian zipper simulations (Fig S3C-D). As expected, the dissipation rate per unit volume is highest in a small region near the contact line (Fig S3C). We integrate to compute the total dissipation rate at each time step, and then plot this as a function of $r_c^2(dr_c/dt)$ to compare it to our approximate analytical prediction from Eq S20 (Fig S3D). When plotted on a log-log axis, this curve shows a linear region with a slope of 2, in agreement with the scaling in Eq S20.

We next estimate the work required to deform the cortex, as given by the second term on the right-hand side of Eq S10. For a spherical cap of contact radius $r_c$ and height $h$:

$$\frac{\partial}{\partial t}\left(\tau \int r ds\right) = \frac{\partial}{\partial t}\left[\tau\left(r_c^2 + \frac{h^2}{2}\right)\right] \tag{S21}$$

Early in spreading, $h$ is approximately constant and tension changes slowly, therefore

$$\frac{\partial}{\partial t}\left[\tau\left(r_c^2 + \frac{h^2}{2}\right)\right] \approx 2\tau r_c \frac{\mathrm{d}r_c}{\mathrm{d}t} \tag{S22}$$

Inserting the approximations from Eq S20 and Eq S22 into the energy balance (Eq S10) and simplifying, we arrive at the following differential equation:

$$r_c^3\left(\frac{\mathrm{d}r_c}{\mathrm{d}t}\right) = \frac{2(\gamma - \tau)}{\Pi_0} \tag{S23}$$

In early spreading, tension changes more slowly than $r_c$; therefore, it can be treated as a constant. This leads to the spreading law observed in our model as well as in a previous computational model of passive cell spreading [2]

$$r_c \propto t^{\frac{1}{4}} \rightarrow A_c \propto t^{\frac{1}{2}} \tag{S24}$$

## Appendix C. Development of $C^1$ versions of tension and protrusion stress relations

Our numerical calculations require versions of the piecewise relationships for tension (Eq 1) and protrusion stress (Eq 11) that have continuous first derivatives. We have developed $C^1$ versions of these relations by using polynomials to transition between each piecewise domain. For tension, we use

$$\tau(A_{cell}) = \begin{cases} 0.01 + 0.16\left(\frac{A_{cell}}{A_{cell,0}} - 1\right)\frac{\mathrm{mN}}{\mathrm{m}} & \text{for } \frac{A_{cell}}{A_{cell,0}} \leq 1.13 \\ 0.7405\left(\frac{A_{cell}}{A_{cell,0}} - 1\right)^2 - 0.0325\left(\frac{A_{cell}}{A_{cell,0}} - 1\right) + 0.0225 & \text{for } 1.13 < \frac{A_{cell}}{A_{cell,0}} \leq 1.39 \\ 0.0516 + 0.545\left(\frac{A_{cell}}{A_{cell,0}} - 1.26\right)\frac{\mathrm{mN}}{\mathrm{m}} & \text{for } \frac{A_{cell}}{A_{cell,0}} > 1.39 \end{cases} \tag{S25}$$

The $C^1$ version of protrusion stress requires two separate transition regions, which we achieve by using cubic polynomials:

$$\sigma_{prot} = \sigma_{prot,max} \begin{cases} \left[0.05 + 0.3\left(\frac{A_c}{A_{c,trans}}\right)\right] \text{ for } \frac{A_{cell}}{A_{cell,0}} \leq 1.13 \\ c_3 A_c^3 + c_2 A_c^2 + c_1 A_c + c_0 \quad \text{for } 1.13 < \frac{A_{cell}}{A_{cell,0}} \leq 1.39 \\ \left[0.35 + 0.65\left(\frac{A_c - A_{c,trans}}{120}\right)^{\frac{1}{2}}\right] \text{ for } \frac{A_{cell}}{A_{cell,0}} > 1.39 \ \& \ A_c \leq A_{c,mid} + 100 \\ d_3 A_c^3 + d_2 A_c^2 + d_1 A_c + d_0 \quad \text{for } A_{c,trans} + 100 < A_c \leq A_{c,trans} + 140 \\ 1 \quad when\ A_c > A_{c,trans} + 140 \end{cases} \tag{S26}$$

The $c$ and $d$ coefficients are found by solving the appropriate linear systems. Their values generally depend on the contact area $A_c$ at different values of surface area deformation; namely, at $A_{cell} = 1.13\ A_{cell,0}$ , $A_{cell} = 1.26\ A_{cell,0}$ , and $A_{cell} = 1.39\ A_{cell,0}$. These are derived from sample runs of the simulation.

## Appendix D. Details of finite element implementation

The governing equations are given in Methods, referred to as the "velocity equation" (Eq 17) and the "pressure equation" (Eq 18) below. Both equations are readily cast into a Galerkin form, which then is rewritten in matrix form as is conventional for finite element methods.

For reference, we give the elemental contributions to the stiffness matrices and load vectors for each finite element system, following the notation used by Hughes [6]. $N_a$ is used to denote the finite element shape function associated with node $a$. We use bilinear quadrilateral shape functions and compute all integrals using two-by-two Gauss quadrature.

The velocity equation (Eq 17) gives rise to the linear system

$$\mathbf{K}\,\mathbf{v}_{all} = \mathbf{F} \tag{S27}$$

The vector $\mathbf{v}_{all}$ contains the velocity values $[v_r, v_z]$ at each node, and the global stiffness matrix $\mathbf{K}$ and global load vector $\mathbf{F}$ are assembled from elemental contributions. The contributions from nodes $a$ and $b$ belonging to element $e$ are given as follows (note the factor of $2\pi r$ due to axial symmetry, as well as the term $(N_a N_b/r^2)$ which arises when computing $\nabla \mathbf{v}$ in cylindrical coordinates)

$$\mathrm{K}_{arbr,e} = \int \left(2\frac{\partial N_a}{\partial r}\frac{\partial N_b}{\partial r} + 2\frac{N_a N_b}{r^2} + \frac{\partial N_a}{\partial z}\frac{\partial N_b}{\partial z}\right) 2\pi r d\Omega \tag{S28}$$

$$\mathrm{K}_{arbz,e} = \int \frac{\partial N_a}{\partial r}\frac{\partial N_b}{\partial z} 2\pi r d\Omega$$

$$\mathrm{K}_{azbr,e} = \int \frac{\partial N_a}{\partial z}\frac{\partial N_b}{\partial r} 2\pi r d\Omega$$

$$\mathrm{K}_{azbz,e} = \int \left(2\frac{\partial N_a}{\partial z}\frac{\partial N_b}{\partial z} + \frac{\partial N_a}{\partial r}\frac{\partial N_b}{\partial r}\right) 2\pi r d\Omega$$

For the load vector

$$\mathrm{F}_{ar,e} = \int p_{est}\left(\frac{\partial N_a}{\partial r} + \frac{N_a}{r}\right) 2\pi r d\Omega + \int N_a \sigma_r 2\pi r d\Gamma \tag{S29}$$

$$\mathrm{F}_{az,e} = \int p\frac{\partial N_a}{\partial z} 2\pi r d\Omega + \int N_a \sigma_z 2\pi r d\Gamma$$

where the second term in the load vector arises from the Neumann boundary condition (stress balance, where $[\sigma_r, \sigma_z]$ are the boundary stresses given by adding the adhesion stress, protrusion stress, and cortical stress) and only appears for those elements which belong to the free boundary of the cell. For elements in contact with the substrate, there is no contribution from the Dirichlet boundary condition as the enforced velocity is equal to zero.

The pressure equation (Eq 18) gives rise to the linear system

$$\mathbf{Q}\,\mathbf{p}_{all} = \mathbf{G} \tag{S30}$$

The vector $\mathbf{p}_{all}$ contains the pressure value $p$ at each node. The global stiffness matrix **Q** and global load vector **G** are assembled from elemental contributions given by

$$\mathrm{Q}_{ab,e} = \int \left[N_a N_b - \epsilon\left(\frac{\partial N_a}{\partial r}\frac{\partial N_b}{\partial r} + \frac{\partial N_a}{\partial z}\frac{\partial N_b}{\partial z}\right)\right] 2\pi r d\Omega \tag{S31}$$

$$\mathrm{G}_{a,e} = \int N_a \left[p_{est} - \frac{\partial v_r}{\partial r} - \frac{v_r}{r} - \frac{\partial v_z}{\partial z}\right] 2\pi r d\Omega \tag{S32}$$

The expression for $\mathrm{G}_a$ incorporates the assumption that $\nabla p \cdot \mathbf{n}$ is zero along the cell boundary, as dictated by the boundary condition, and $\nabla^2 p = 0$ everywhere, which is satisfied exactly for an incompressible fluid. Derivatives of $[v_r, v_z]$ are computed using bilinear quadrilateral shape functions.

This system of equations is solved iteratively, as described in Methods. Examples of the fluid velocities and pressures obtained by the Brownian zipper model (Fig S4A) and the protrusive zipper model (Fig S4B) are included for illustration.

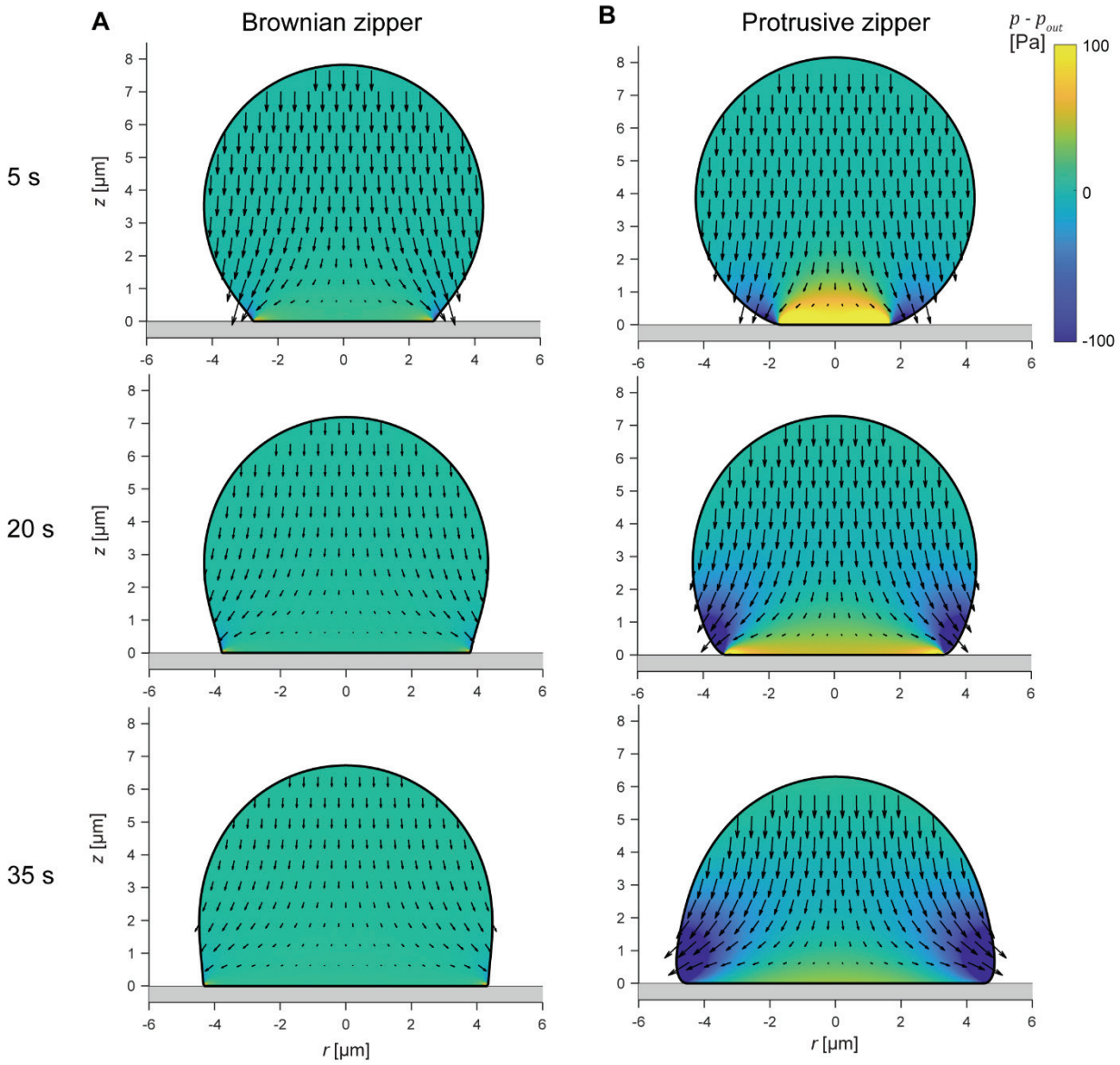


**Fig S4. Example velocity and pressure fields obtained by finite element computations.**
(A) Fluid velocity vector fields and pressure scalar fields (heat maps) are shown for purely adhesion-driven spreading with a ligand density of 10%. The magnitude of fluid velocities decay relatively quickly over time and the highest pressures are localized to the contact line in early spreading. (B) Fluid velocity vector fields and pressure scalar fields (heat maps) are shown for purely protrusion-driven spreading. The velocities remain of similar magnitude over time due to the time-dependent increase in protrusion stress.

## Appendix E. Numerical testing and optimization

The accuracy of numerical computations such as used in this study can be affected by several factors. In this appendix, we document a number of tests that we have carried out to verify the reliability of our numerical predictions. All tests of the Brownian zipper model are conducted for a ligand density ($\rho_l$) of 10%, and all tests of the protrusive zipper model are carried out in the absence of adhesion stress.

### I. Test for incompressibility

Solving the governing equations for the perturbed Stokes equations given in Methods (Eqs 17 and 18) yields an approximate satisfaction of incompressibility. The degree to which incompressibility is enforced depends on the magnitude of the perturbation parameter $\epsilon$ in Eq 18. Specifically, as $\epsilon$ goes to zero, the fluid becomes more incompressible. However, if $\epsilon$ is too small, there are numerical difficulties. Thus, it is worthwhile to evaluate how closely incompressibility is satisfied for different values of $\epsilon$. In our model, $\epsilon$ scales with the characteristic radius of an individual element $h_{mesh}$ and the effective viscosity $\mu$ [7]. As described in Eq 15 of the main text, we generally require that $\epsilon \leq h_{mesh}^2/\mu$ , but we can write more generally

$$\epsilon = \bar{\epsilon}\left(\frac{h_{mesh}^2}{\mu}\right) \tag{S33}$$

where $\bar{\epsilon}$ is a dimensionless scaling factor which should have a magnitude less than or equal to one to satisfy the above inequality. Here, we assess how this parameter affects the error in our model.

We quantify the degree of compressibility at different locations in the cell body in terms of the local rate of dilatation, obtained by integrating $\nabla \cdot \mathbf{v}$ over individual elements and dividing by the element volume $V_{el}$. That is,

$$\text{Dilatation rate } = \frac{\iiint (\nabla \cdot \mathbf{v}) dV}{V_{el}} \tag{S34}$$

This dilatation rate has units of inverse seconds and describes the rate of fluid expansion per unit volume. In general, we expect the largest departures from perfect incompressibility to occur in the immediate vicinity of the perimeter of the contact region, due to a well-known singularity that has been examined thoroughly for different cases of droplet spreading [4]. Focusing on this region, we have characterized how our choice of the value of $\epsilon$ (Eq S33) affects the dilatation rate (Fig. S5A). We evaluate the overall error of the model in terms of the mean square error (MSE) for the incompressibility condition

$$\text{MSE} = \frac{\iiint (\nabla \cdot \mathbf{v})^2 dV}{V_{tot}} \tag{S35}$$

The MSE initially depends only weakly on the value of $\epsilon$, but increases considerably at higher values, as expected (Fig S5B-C). Generally, a value of $\bar{\epsilon} = 1$ results in sufficiently low error while also avoiding numerical difficulties associated with lower values of $\bar{\epsilon}$.

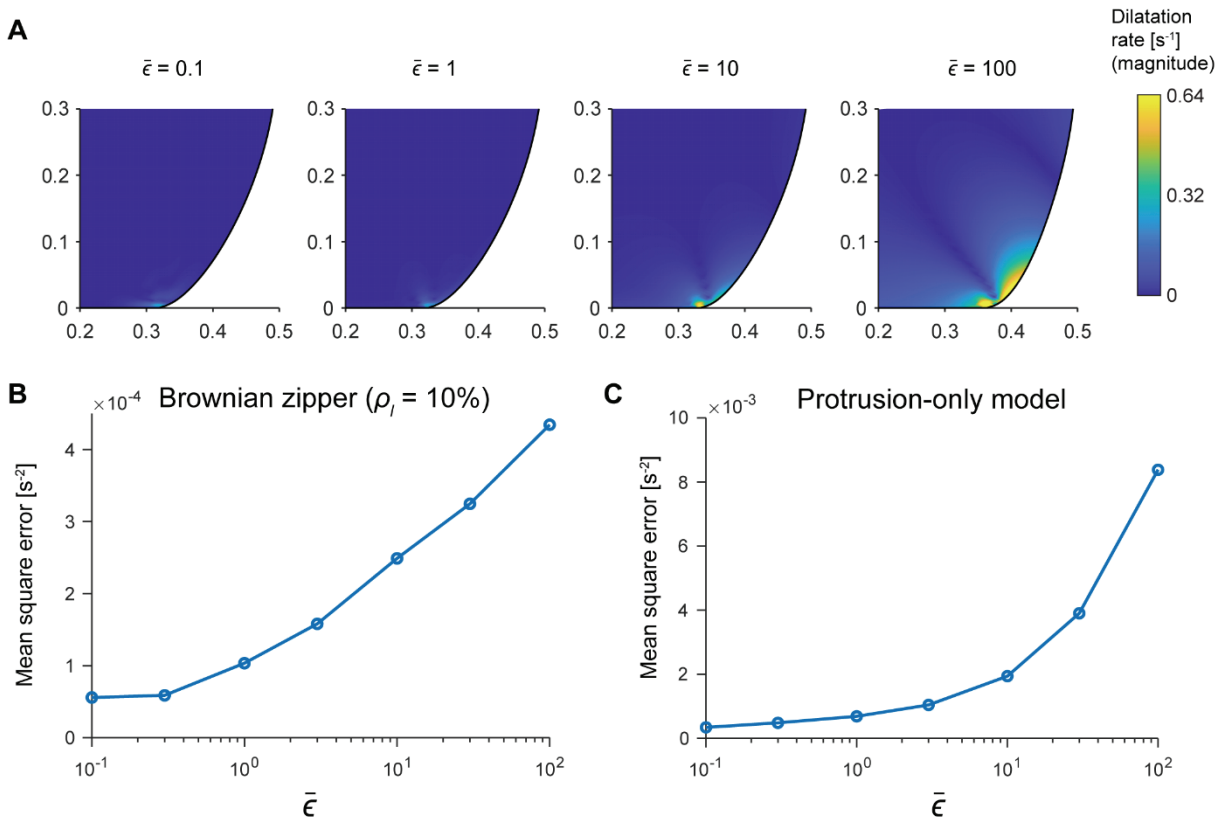


**Fig S5. Testing for incompressibility.**
(A) Heat maps of the dilatation rate within the leading edge of the cell for purely protrusion-driven spreading at $t$ = 15s for different values of $\bar{\epsilon}$. (B) Volumetric mean square error is plotted as a function of $\bar{\epsilon}$ for Brownian Zipper simulations at $t$ = 15 s. (C) Volumetric mean square error is plotted as a function of $\bar{\epsilon}$ for protrusion-only spreading at 15 s.

## II. Time-step testing

The optimal time step $\Delta t$ for many fluid mechanics simulations depends on the fluid velocity and the mesh resolution. A common reference for this is the Courant number, generally given by

$$C = \frac{v\Delta t}{l} \tag{S36}$$

where $l$ is a characteristic length and $v$ is a characteristic velocity. For numerical stability, $C$ should be much less than one.

We use Eq S36 to determine the appropriate time step for the minimum ratio of $l/v$ across all elements, that is

$$\Delta t = C \min\left(\frac{l}{v}\right) = C \min_{\text{all el}}\left(\min\left[\frac{r_{span}}{v_{r,c}}, \frac{z_{span}}{v_{z,c}}\right]\right) \tag{S37}$$

where $r_{span}$ is the span of the element in the $r$ direction, $z_{span}$ is the span of the element in the $z$ direction, $[v_{r,c}, v_{z,c}]$ is the velocity vector at the centroid of the element, and $C$ is the desired Courant number. For instance, if $C = 0.1$, fluid flow crosses at most 10% of any individual element during a single time step. We performed a series of simulations using decreasing values of $C$ to establish at which Courant number our computations converge satisfactorily. Figure S6 shows examples of testing different time steps for the Brownian Zipper model (Fig S6A) and the protrusive zipper model with no adhesion stress (Fig S6B). For smaller time steps, the contact area curves become smoother and converge to a single solution. Generally, we find that $C \leq 0.1$ performs well in these cases, which is the value we choose for our simulations.

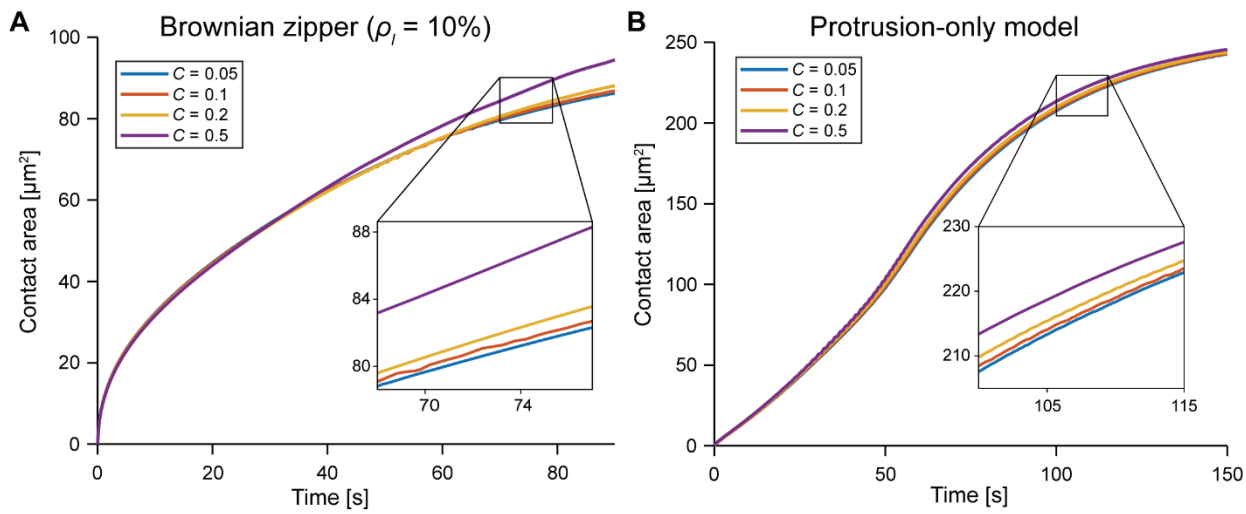


**Fig S6. Time-step testing.**
Contact area versus time for different Courant numbers for (A) the Brownian zipper model and (B) purely protrusion-driven spreading.

## III. Mesh refinement

We ensured that the results of our simulations do not depend significantly on the mesh resolution as follows. When constructing the mesh, we start by specifying the boundary nodes, choosing tight spacing near the substrate and gradually increasing spacing to 0.17 μm over the rest of the cell contour (Fig S7A). After parameterizing the contour, we use transfinite interpolation to construct the interior mesh ([8], Fig S7A). Using a global edge spacing of 0.17 μm generally results in about 2,000 elements. Here, we focus on refining the mesh spacing close to the surface where the stresses are most concentrated.

For both the Brownian zipper model and the protrusive zipper model, we tested minimum boundary point spacing values $\Delta s_{min}$ of 25 nm, 10 nm, 5 nm, and 2.5 nm. In both cases, we find

convergence for $\Delta s_{min} \leq 5$ nm (Fig S7B-C). For our simulations in the main paper, we use $\Delta s_{min}$ = 2.5 nm.

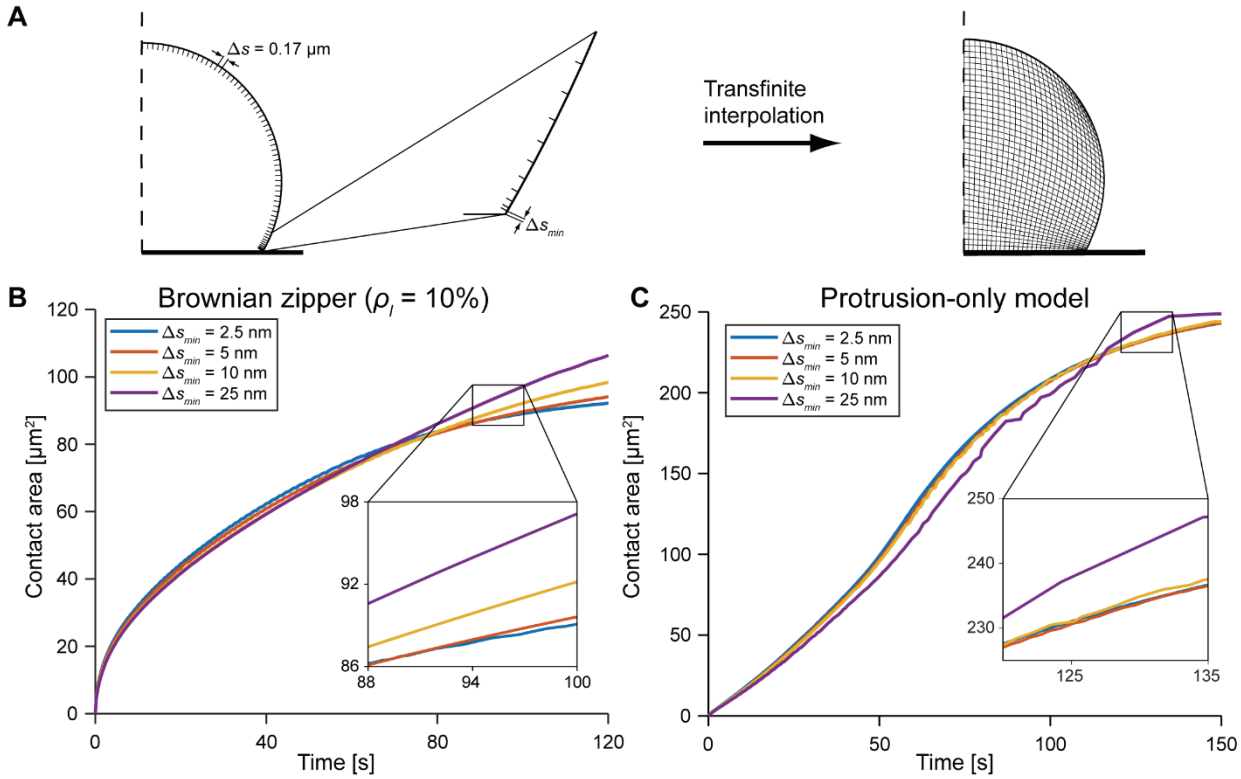


**Fig S7. Mesh refinement.**
(A) Illustration of mesh construction including our choice of relevant boundary spacing intervals. Convergence of the simulations is evaluated by inspection of contact-area-versus-time curves obtained with different minimum mesh spacings close to the substrate ($\Delta s_{min}$) for (B) the Brownian zipper model and (C) purely protrusion-driven spreading.

## References


1. Sukumaran S, Seifert U. Influence of shear flow on vesicles near a wall: A numerical study. Phys Rev E. 2001;64(1). doi: ARTN 011916 DOI 10.1103/PhysRevE.64.011916. PubMed PMID: WOS:000169907100090.
2. Etienne J, Duperray A. Initial dynamics of cell spreading are governed by dissipation in the actin cortex. Biophys J. 2011;101(3):611-21. Epub 2011/08/03. doi: 10.1016/j.bpj.2011.06.030. PubMed PMID: 21806929; PubMed Central PMCID: PMCPMC3145312.
3. Maenaka K, van der Merwe PA, Stuart DI, Jones EY, Sondermann P. The human low affinity Fcgamma receptors IIa, IIb, and III bind IgG with fast kinetics and distinct thermodynamic properties. J Biol Chem. 2001;276(48):44898-904. Epub 2001/09/07. doi: 10.1074/jbc.M106819200. PubMed PMID: 11544262.
4. Bonn D, Eggers J, Indekeu J, Meunier J, Rolley E. Wetting and spreading. Reviews of Modern Physics. 2009;81(2):739-805. doi: 10.1103/RevModPhys.81.739. PubMed PMID: WOS:000267197500008.
5. Aris R. Vectors, Tensors, and the Basic Equations of Fluid Mechanics: Dover Publications, Inc.; 1962.
6. Hughes TJR. The Finite Element Method: Linear Static and Dynamic Finite Element Analysis: Dover; 2000.
7. Drury JL, Dembo M. Hydrodynamics of micropipette aspiration. Biophys J. 1999;76(1 Pt 1):110-28. Epub 1999/01/06. doi: 10.1016/S0006-3495(99)77183-3. PubMed PMID: 9876128; PubMed Central PMCID: PMCPMC1302505.
8. Knupp PS, S.L. The Fundamentals of Grid Generation. 1st ed: CRC Press; 1993.

# S7 Table. Modeling parameters

| Parameter | Description | Value | Notes |
|---|---|---|---|
| $\tau_0$ | Resting cortical tension | 0.01 mN/m | Matches experimental value used by Herant et al [1] |
| $\tau_{max}$ | Maximum cortical tension | ~1 mN/m | In a reasonable range for high tensions measured during neutrophil phagocytosis [2, 3] |
| $\mu$ | Effective cytoplasmic viscosity | 200 Pa-s (passive)<br>1,660 Pa-s (active) | Matches experimentally measured values [4, 5] |
| $R_0$ | Initial cell radius | 4.25 μm | Radius of a human neutrophil |
| $\sigma_0$ | Adhesion stress constant (scaling factor) | 370 Pa | Together with the ligand density, this determines the adhesion strength |
| $\rho_{IgG,max}$ | Ligand density corresponding to 100% for Brownian Zipper model | 10,000 IgG/μm$^2$ | This density corresponds to about $600\ \mu\mathrm{J/m^2}$, which exceeds values derived from other cases of cell spreading [6] |
| $D_0$ | Zero adhesion force distance | 50 nm | Relatively large distance required for mesoscopic model, as standard in other continuum models [7, 8] |
| $\sigma_{prot,max}$ | Max. protrusion stress | 3,500 Pa | Actin filaments growing in parallel can achieve forces above 1 nN per μm$^2$ (> 1 kPa) [9, 10] |
| $s_0$ | Protrusive force range | 0.8 μm | Controls how the protrusion stress decays along the membrane (Eq 8) |
| $t_0$ | Characteristic time for decay of protrusion stress | 66 s | Used for discrete adhesion model (Eq 13) |

# References


1. Herant M, Lee CY, Dembo M, Heinrich V. Protrusive push versus enveloping embrace: computational model of phagocytosis predicts key regulatory role of cytoskeletal membrane anchors. PLoS Comput Biol. 2011;7(1):e1001068. doi: 10.1371/journal.pcbi.1001068. PubMed PMID: 21298079; PubMed Central PMCID: PMCPMC3029235.
2. Lee CY, Thompson GR, 3rd, Hastey CJ, Hodge GC, Lunetta JM, Pappagianis D, et al. Coccidioides Endospores and Spherules Draw Strong Chemotactic, Adhesive, and Phagocytic Responses by Individual Human Neutrophils. PLoS One. 2015;10(6):e0129522. doi: 10.1371/journal.pone.0129522. PubMed PMID: 26070210; PubMed Central PMCID: PMCPMC4466529.
3. Herant M, Heinrich V, Dembo M. Mechanics of neutrophil phagocytosis: behavior of the cortical tension. J Cell Sci. 2005;118(Pt 9):1789-97. doi: 10.1242/jcs.02275. PubMed PMID: 15827090.
4. Evans E, Yeung A. Apparent viscosity and cortical tension of blood granulocytes determined by micropipet aspiration. Biophys J. 1989;56(1):151-60. Epub 1989/07/01. doi: 10.1016/S0006-3495(89)82660-8. PubMed PMID: 2752085; PubMed Central PMCID: PMCPMC1280460.
5. Tran-Son-Tay R, Needham D, Yeung A, Hochmuth RM. Time-dependent recovery of passive neutrophils after large deformation. Biophys J. 1991;60(4):856-66. Epub 1991/10/01. doi: 10.1016/S0006-3495(91)82119-1. PubMed PMID: 1742456; PubMed Central PMCID: PMCPMC1260136.
6. Cuvelier D, Thery M, Chu YS, Dufour S, Thiery JP, Bornens M, et al. The universal dynamics of cell spreading. Curr Biol. 2007;17(8):694-9. Epub 2007/03/24. doi: 10.1016/j.cub.2007.02.058. PubMed PMID: 17379524.
7. Sukumaran S, Seifert U. Influence of shear flow on vesicles near a wall: A numerical study. Phys Rev E. 2001;64(1). doi: ARTN 011916 DOI 10.1103/PhysRevE.64.011916. PubMed PMID: WOS:000169907100090.
8. Etienne J, Duperray A. Initial dynamics of cell spreading are governed by dissipation in the actin cortex. Biophys J. 2011;101(3):611-21. Epub 2011/08/03. doi: 10.1016/j.bpj.2011.06.030. PubMed PMID: 21806929; PubMed Central PMCID: PMCPMC3145312.
9. Parekh SH, Chaudhuri O, Theriot JA, Fletcher DA. Loading history determines the velocity of actin-network growth. Nat Cell Biol. 2005;7(12):1219-23. Epub 2005/11/22. doi: 10.1038/ncb1336. PubMed PMID: 16299496.
10. Marcy Y, Prost J, Carlier MF, Sykes C. Forces generated during actin-based propulsion: a direct measurement by micromanipulation. Proc Natl Acad Sci U S A. 2004;101(16):5992-7. Epub 2004/04/14. doi: 10.1073/pnas.0307704101. PubMed PMID: 15079054; PubMed Central PMCID: PMCPMC395911.